Digital design of multimaterial photonic particles

Guangming Tao[a], Joshua J. Kaufman[a], Soroush Shabahang[a], Roxana Rezvani Naraghi[a,b], Sergey V. Sukhov[a], John D. Joannopoulos[c], Yoel Fink[c], Aristide Dogariu[a], and Ayman F. Abouraddy[a,1]

[a]CREOL, The College of Optics and Photonics, University of Central Florida, Orlando, FL 32816; [b]Department of Physics, University of Central Florida, Orlando, FL 32816; and [c]Research Laboratory of Electronics, Massachusetts Institute of Technology, Cambridge, MA 02139

Edited by Federico Capasso, Harvard University, Cambridge, MA, and approved May 6, 2016 (received for review February 2, 2016)

Scattering of light from dielectric particles whose size is on the order of an optical wavelength underlies a plethora of visual phenomena in nature and is a foundation for optical coatings and paints. Tailoring the internal nanoscale geometry of such "photonic particles" allows tuning their optical scattering characteristics beyond those afforded by their constitutive materials—however, flexible yet scalable processing approaches to produce such particles are lacking. Here, we show that a thermally induced in-fiber fluid instability permits the "digital design" of multimaterial photonic particles: the precise allocation of high refractive-index contrast materials at independently addressable radial and azimuthal coordinates within its 3D architecture. Exploiting this unique capability in all-dielectric systems, we tune the scattering cross-section of equisized particles via radial structuring and induce polarization-sensitive scattering from spherical particles with broken internal rotational symmetry. The scalability of this fabrication strategy promises a generation of optical coatings in which sophisticated functionality is realized at the level of the individual particles.

multimaterial fibers | particles | optical scattering | fluid instabilities

The prospect of exercising complete control over the internal 3D structure of multimaterial microparticles and nanoparticles produced in a scalable fashion has profound implications for scientific disciplines ranging from photonics (1, 2) to biomedicine (3–5), and for a multitude of industrial applications, such as cosmetics, sunscreen lotions, optical coatings, and paints (6–8). For example, most paints are emulsions containing dielectric "photonic particles" designed to optimize optical scattering through judicious selection of size—typically on the order of an optical wavelength—and refractive index (9). Further tailoring their scattering characteristics requires tuning an internal high refractive-index contrast nanoscale architecture, which remains an outstanding fabrication challenge despite recent progress (10–14). Indeed, the process kinetics in bottom-up and top-down particle fabrication strategies impose fundamental constraints on the extent of structural control and the magnitude of refractive-index contrast. To date, there is no viable approach for what may be termed "digital design" of a photonic particle: the precise placement of disparate materials compartmentalized at independently addressable coordinates within a particle at the scale of an optical wavelength. Such structural control is envisioned to introduce entirely new optical functionalities that exploit the particle's resonances (15), such as the elimination of backscattering and increasing the directionality of optical scattering (16–20). Nevertheless, mapping out the phase function of a single isolated photonic particle—to verify its functionality without ensemble averaging—has proven so far to be prohibitively difficult, leading to measurements being carried out on scaled-up particles at longer wavelengths [typically in the microwave spectrum (15)].

Due to the inherent difficulty in achieving such digital design of photonic particles, efforts have been directed instead at structuring the morphology of surfaces to manipulate the scattering of light. Efforts in this direction range from exploiting planar photonic crystals to plasmonic structures and metasurfaces to control the directionality of optical scattering (21–23) or optical polarization (24), and even achieve zero refractive index (25). These patterned surfaces typically involve a large array of elements that—combined—achieve the desired optical functionality. Moreover, many of these structures use metallic components that introduce unwanted optical losses.

We present here a scalable fabrication strategy for engineering the internal geometry of all-dielectric multimaterial photonic particles, which provide access to sophisticated optical scattering capabilities. The key to addressing the challenge of particle digital design is exploiting a recently discovered in-fiber fluid instability (26–28) that produces spherical particles having—in principle—arbitrary internal structure. A centimeter-scale axisymmetric cylindrical "core" rod is assembled as a prototype of the intended particle structure in a LEGO-like procedure from prefabricated segments of different materials, which is then embedded in a cladding matrix to form a "preform" (29–31). A fiber that is thermally drawn from this preform with reduced transverse feature size defines the initial conditions for a cylinder-to-sphere geometric transformation by thermally inducing the Plateau–Rayleigh capillary instability (PRI) (32, 33) at the heterogeneous interfaces along the whole fiber length (26–28). Because the geometric morphing associated with this fluid instability is predictable, the axially symmetric core is converted into spherical particles with a target architecture that follows from the macroscopic preform structure. The uniqueness and versatility of this processing strategy is brought out here by realizing (*i*) radial control in multilayered particles with predictable layer thicknesses, (*ii*) azimuthal control in particles with discrete rotational symmetry, and (*iii*) combined radial and azimuthal engineering in four-material core–shell particles having Janus core and shell with well-controlled relative orientation of the azimuthally structured layers.

The efficacy of digitally designed photonic particles for rationally controlling optical scattering is confirmed via two key experiments. First, we tailor the radial structure of a high-index contrast all-dielectric core–shell particle to tune the optical scattering

Significance

We present an approach for the facile fabrication of dielectric particles having the size of an optical wavelength yet endowed with a complex multimaterial internal nanoscale architecture. This methodology amounts to "digitally designing" the particle by precisely allocating the desired material at prescribed coordinates within the 3D volume of the particle. The digital design of such a photonic particle enables sophisticated strategies for controlling light scattering. As an example, without changing the size of a core–shell particle, its optical scattering strength can be tuned above or below that afforded by its constitutive materials by changing the core–shell diameter ratio. This work may lead to the development of new optical coatings and paints with exotic functionality.

Author contributions: G.T., J.D.J., Y.F., A.D., and A.F.A. designed research; G.T., J.J.K., S.S., R.R.N., and S.V.S. performed research; G.T., R.R.N., S.V.S., A.D., and A.F.A. analyzed data; and G.T., R.R.N., A.D., and A.F.A. wrote the paper.

The authors declare no conflict of interest.

This article is a PNAS Direct Submission.

[1]To whom correspondence should be addressed. Email: raddy@creol.ucf.edu.

This article contains supporting information online at www.pnas.org/lookup/suppl/doi:10.1073/pnas.1601777113/-/DCSupplemental.

cross-section—without changing the particle size—to reach values above or below that of equally sized particles of the constitutive materials. This feature is verified through mapping out—for the first time (to our knowledge)—the phase function of a single photonic particle by combining evanescent field excitation with near-field optical scanning microscopy, instead of relying on an ensemble measurement. Second, we verify that breaking the internal rotational symmetry of a particle with spherical external morphology produces polarization-dependent scattering. Exploiting the scale invariance of our fabrication strategy (27), we first produce in both cases larger-scale particles (~10–40 μm in diameter) to confirm the internal structure through direct structural and compositional imaging, and then carry out the optical experiments on reduced-scale photonic particles in which the structure is established through single-particle optical scattering. Such particles may serve as designer optical scattering elements for constructing new synthetic photonic materials and structures.

Results

In-Fiber Fabrication Strategy. The starting point of our fabrication methodology (shown schematically in Fig. 1) is the construction of a centimeter-scale preform prepared using macroscopic processes, such as extrusion (34), casting, etc. (*SI Appendix*). This preform contains a prototype of the targeted particle architecture in the form of a multimaterial cylindrical core assembled from preshaped segments of the desired materials (Fig. 1 *A* and *B*). The core is embedded in an amorphous cladding that facilitates thermal drawing into a fiber (Fig. 1*C*), thereby reducing the core diameter to the scale of the intended particle size (27)—potentially ranging from millimeters down to tens of nanometers (27, 35). Surface energy at the core-cladding interface, and at interfaces within the core itself, is exploited to initiate the PRI upon reducing the viscosity via thermal treatment (26). The result is a thermally induced emulsification of the whole core length, thereby morphing it into an ordered and oriented necklace of structured spherical particles (26) to be released from the fiber through selective dissolution of the cladding (Fig. 1*D*). The dynamics of the breakup process is shown in Movie S1, where six parallel cores in a fiber are thermally treated and undergo a physical transformation from microthreads to a 2D array of spheres. We focus here on thermally compatible combinations of polymers (28) and soft glasses (26, 27, 36, 37) that afford high optical refractive-index contrasts, but a broader range of materials can be exploited in this process, such as crystalline semiconductors including silicon and germanium (38) and even globular biomaterials (28).

Examples of preform cross-sections produced by multimaterial coextrusion (34) are presented in Fig. 1 *E–G* (*SI Appendix*, *S1: Overview of the Preform Preparation Process* and *S2: Structured-Preform Fabrication*): first, a preform core composed of alternating cylindrically nested layers of a glass (G, As_2S_3) and a polymer [P, polyethersulfone (PES)]; second, a core with broken azimuthal symmetry formed of two glasses [G_1, As_2S_3; G_2, $Ge_{1.3}(As_2Se_3)_{98.7}$] assembled from wedged segments; and third, a core combining radial and azimuthal structural engineering, consisting of a glass–core/polymer–shell geometry in which both layers have a Janus structure—thus juxtaposing four materials. Uniquely, the different layers with broken rotational symmetry in the last example may be oriented at will with respect to each other. These selected examples highlight the potential for digitally designing the cylindrical core prototype, which is facilitated by its large size. We now proceed to show that a thermally induced PRI-driven process in fibers drawn from these preforms indeed produces particles with the desired geometry and associated optical functionality.

Control over the Radial Structure. The initial conditions for in-fiber fabrication of spherical multilayered particles are defined by a fiber core with nested layers. Because the instability growth time—as described in the classical Tomotika model—is linear in the diameter of the cylindrical interface between two viscous fluids (39), the cylindrical multilayer core structure (Fig. 2*A*) breaks up from the innermost layer outward (Fig. 2*B*) and yields multilayered spherical particles upon heating the fiber (Fig. 2 *C* and *D*). The feasibility of this strategy is established by direct imaging of microparticle realizations with increasing number of layers, starting from a unimaterial glass particle (Fig. 2 *E* and *I*) to a five-layer particle with alternating glass and polymer shells (Fig. 2 *H* and *L*). Micrographs of the harvested particles after sectioning them at midplane reveal smooth, sharp interfaces, and the integrity of the extracted particles after selective dissolution of the polymer cladding—using a solvent that is detrimental to exposed internal structures—indicates that the spherical-shell layers form in an orderly sequence (from the inside out) without pinching. Furthermore, the spherical symmetry and concentricity of the internal particle interfaces (Fig. 2 *I–L*) is markedly improved with respect to those in the initial fiber (Fig. 2 *E–H*), thereby confirming a theoretical prediction that perturbations in the fiber core are smoothed out during the surface-tension–driven breakup process (40)—which relaxes the fabrication tolerances at the preform and fiber levels.

Although the thicknesses of the layers in the particle are related deterministically to those of the cylindrical shells in the drawn fiber (28, 40), the dynamics of the PRI nevertheless constrains the relative shell diameters for which the breakup results in the intended layered structure. It is well established from the classic Tomotika model that the breakup period of a viscous thread embedded in a viscous matrix is proportional to the diameter of the thread (39). The breakup period is related to the instability wavelength having the highest growth rate. If the core diameter is much smaller than that of the shell $d_{core}/d_{shell} \ll 1$, then the resulting breakup period of the core may—in turn—be significantly smaller than that of the shell.

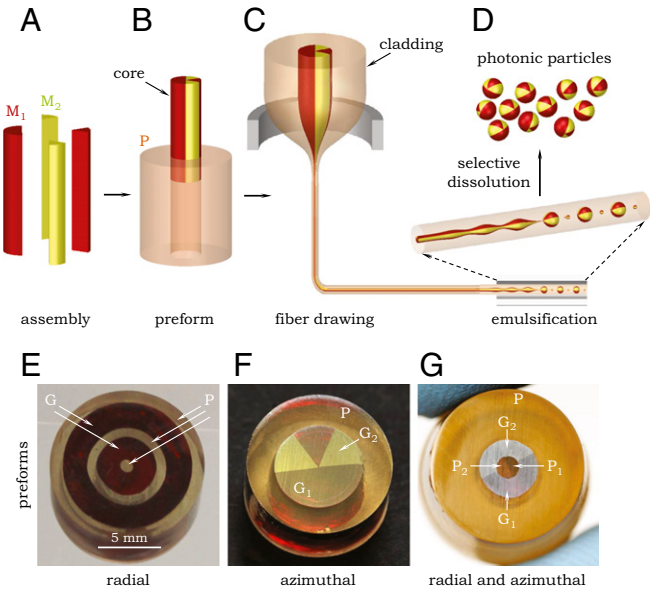

Fig. 1. General strategy for the digital design of multimaterial photonic particles independently in the radial and azimuthal directions. (*A*) Segments of two materials, M_1 and M_2, are produced that may be assembled into an axisymmetric cylinder or core. (*B*) The core is provided with a polymer (P) cladding to form a preform. (*C*) The preform is thermally drawn into an extended continuous fiber that is subsequently heated leading to well-ordered and oriented emulsification of the core: its breakup into spheres in a low-viscosity state driven by surface tension. (*D*) The particles are harvested by selective dissolution of the cladding. (*E–G*) Optical micrographs of preform cross-sections showing (*E*) radial control in a multilayer structure (G, As_2S_3; and P, PES), (*F*) azimuthal control with broken rotational symmetry [G_1, As_2S_3; G_2, $Ge_{1.3}(As_2Se_3)_{98.7}$; and P, PES], and (*G*) control over the combined radial and azimuthal geometry [G_1, As_2S_3; G_2, $Ge_{1.3}(As_2Se_3)_{98.7}$; P_1, PES; P_2, PEI; and P, PES]. Fibers produced from the preforms in *E–G* are shown in Figs. 2, 4, and 5, respectively.

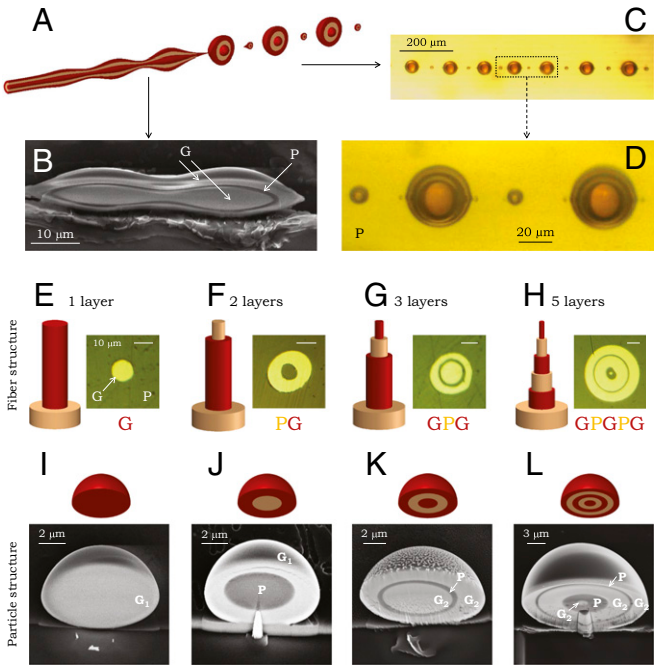

Fig. 2. Control over particle structure in the radial direction. (*A*) Schematic of a fiber containing a cylindrical core consisting of nested shells undergoes the PRI-driven breakup into spherical multilayer particles. The cladding is not shown for clarity. (*B*) SEM micrograph of a three-layer core sectioned using a focused ion beam (FIB) with the PRI arrested before complete breakup of the core (G, As_2S_3; and P, PES). (*C* and *D*) Optical transmission micrographs of five-layer particles after breakup held in the polymer (P) cladding separated by smaller multilayered satellite particles. (*E*–*H*) Optical reflection micrographs of fiber multilayered-core cross-sections (G, As_2S_3; and P, PES). Schematics of the fiber structures are also shown. (*I*–*L*) SEM micrographs of multilayer particles after sectioning with a raster-scanning low-current FIB. Schematic of the particles are shown above each panel. G_1, As_2S_3; G_2, $Ge_{1.3}(As_2Se_3)_{98.7}$; P, PES.

Consequently, instead of the desired core–shell structure, multiple smaller core particles forming a linear chain extending between the antipodes of the particle are obtained inside a single shell (28, 40).

We confirm these predictions experimentally (*SI Appendix*, Fig. S12) by inducing the PRI-driven breakup in PES–core, As_2S_3–shell structures that differ in the ratio of the core-to-shell diameters d_{core}/d_{shell}. First, when $d_{core}/d_{shell}=0.7$, the sinusoidal modulations resulting from the PRI along the interfaces occur simultaneously upon heating and the target core–shell structure is obtained. Second, with $d_{core}/d_{shell}=0.5$, the modulation along the interfaces are independent to some degree, and we obtain a subset of particles in which the core–shell structure does not develop. Instead, we sometimes obtain two core particles within the shell. Third, with $d_{core}/d_{shell}=0.2$, the growth of the PRI-induced modulations along the interfaces are independent and the core breaks up into spherical particles before the shell breaks up altogether. Consequently, the shells after formation contain several core particles. Furthermore, the satellite particles are formed of the shell material only. The crossover that occurs between the stable (core–shell) and unstable (multiple cores in a shell) regimes at $d_{core}/d_{shell}\approx 0.5$ is borne out by calculations based on a linear stability analysis (28) and direct fluid-dynamical simulations (40). The potential for forming strings of particles along the axis of a larger particles is exploited below in inducing polarization-sensitive optical scattering.

Control over the Optical Scattering Efficiency in Core–Shell Particles. To date, tailoring the optical scattering efficiency Q_{sca} [defined as the ratio of the scattering to geometric cross-sections (41)] from particles have relied on either changing their size or refractive index. Realizing high Q_{sca}, as necessary, for example, in optical coatings to achieve opacity in thin layers without absorption, typically necessitates increasing the refractive index, an approach fundamentally limited by naturally available materials (42). We proceed to show here that multilayer dielectric particles with controlled radial structure and high refractive-index contrast (without incorporating metals) enable rational control over Q_{sca} solely through the internal architecture. This point is made clear through a calculation of Q_{sca} at a wavelength $\lambda=532$ nm for a core–shell particle of fixed radius $a=500$ nm (polymer–core and glass–shell refractive indices are $n_c=1.5$, $n_s=2.51+i0.28$, respectively), which reveals a modulation in Q_{sca} while varying the core radius r_c between two limits: an all-glass particle ($r_c=0$) and an all-polymer particle ($r_c=a$) (Fig. 3*A*). Thus, by adjusting an internal geometric degree of freedom, Q_{sca} may be varied below or above that of equisized unimaterial particles made of either of the constitutive materials, as a result of multipolar interferences [$ka=(2\pi/\lambda)a\approx 6$].

We confirm these theoretical predictions by examining specifically designed and manufactured particles having three different core–shell ratios, structures A ($r_c=0$ nm), B ($r_c=325$ nm), and C ($r_c=400$ nm) highlighted in Fig. 3*A*, and selected to confirm that varying r_c can reduce or enhance Q_{sca}. Critically, to isolate the effect of the internal particle structure on Q_{sca} and eliminate the impact of

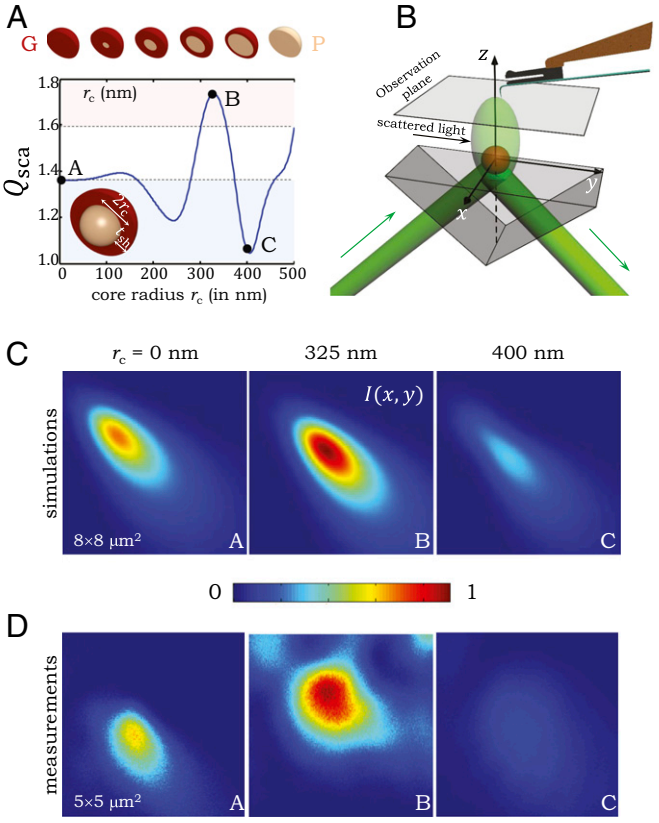

Fig. 3. Tailoring the scattering cross-section in high refractive-index contrast core–shell photonic particles. (*A*) Calculated Q_{sca} for a core–shell particle of fixed outer radius 500 nm; core is the polymer (P) PES having radius r_c, whereas the shell is the glass (G) As_2S_3 (refractive indices given in text). Wavelength used in the calculations is 532 nm. (*B*) Schematic of the optical system for dark-field near-field optical scanning microscope (NSOM), which is based on a Nanonics MultiView 4000 NSOM working in standard collection mode. (*C*) Calculated scattered field intensities from three particle structures corresponding to cases A, B, and C in *A*. (*D*) Measured intensity distributions corresponding to those in *C*.

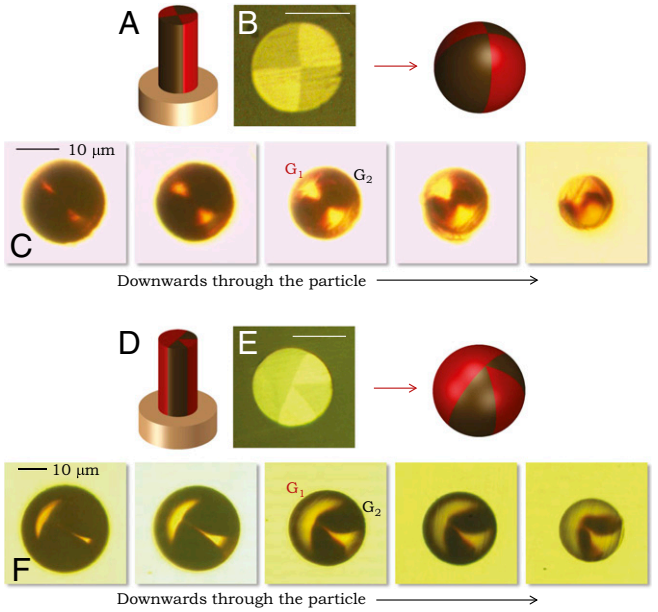

Fig. 4. Control over the azimuthal structure. (*A*–*C*) Beach ball particle with fourfold discrete rotational symmetry. (*A*) Schematic of the fiber structure; (*B*) optical reflection micrograph of the fiber cross-section and schematic of the resulting particle; and (*C*) optical transmission micrographs through a single particle while polishing axially through it. (*D*–*F*) Same as *A*–*C* for a spherical particle lacking rotational symmetry, produced by reversing one sextant (from G_2 to G_1) in a structure with sixfold discrete rotational symmetry. Throughout, G_1, As_2S_3; G_2, $Ge_{1.3}(As_2Se_3)_{98.7}$; and P, PES.

particle–particle interactions, we carry out the measurements on one single particle. The formidable challenge of identifying the extremely weak scattered signal off a single particle from the strong background of incident light is addressed by constructing a dark-field light-scattering setup in which the particle is excited by an evanescent optical field at a wavelength of 532 nm (Fig. 3*B*; *Methods*). Measurements of the scattering phase functions for structures A, B, and C are plotted in Fig. 3*D*. The measurements presented in Fig. 3*D* are "absolute" in the sense that the same intensity scale is used for the three particles. Although symmetry in standard Mie scattering based on propagating plane wave excitation excludes any cross-polarization terms in the scattering matrix, the exponentially decreasing amplitude in the evanescent-wave–scattering arrangement introduces an asymmetry that leads to cross-polarization terms. Consequently, the scattered intensity depends on the specific polarization and direction of the incident beam. The results shown in Fig. 3*D* correspond to *p*-polarized incidence.

To model this evanescent excitation scenario, the usual Mie theory (41)—describing scattering of a propagating electromagnetic plane wave from spherical particles—falls short. Although previous modeling attempts either generalize Mie theory or rely on purely computational techniques (43, 44), we make use instead of a recent theoretical advance in which the conventional Mie theory is directly applied to scattering of evanescent waves through a complex-angle rotation of the standard Mie solution (45, 46). By rotating both the direction and the distribution of the incident electric $\vec{E}(\vec{r}) = \hat{R}_y(-\gamma)\vec{E}\,[\hat{R}_y(\gamma)\vec{r}\,]$ and magnetic $\vec{H}(\vec{r}) = \hat{R}_y(-\gamma)\vec{H}\,[\hat{R}_y(\gamma)\vec{r}\,]$ fields by a complex angle γ, a z-propagating plane wave can be transformed into an evanescent field (46); here, $\vec{E}$, $\vec{H}$, and $\vec{r}$ are electric field, magnetic field, and position vectors, respectively, and $\hat{R}_y(\gamma)$ is a vector-rotation operator around the y axis by an angle γ. By exploiting this complex-angle rotation methodology to calculate the field scattered by spherical core–shell particles excited by the evanescent-field configuration in Fig. 3*B*, we predict the scattered intensity distribution $I(x,y)$ in a plane 2 μm above the particle (Fig. 3*C*), which is in excellent agreement with the measurements (Fig. 3*D*).

Engineering the Azimuthal Structure. Structuring a spherical particle azimuthally—rather than radially—has traditionally been a more demanding fabrication task, and to date is limited to "Janus" structures in polymers in which two materials are compartmentalized in two hemispheres or only the surface is treated (47–49). Although symmetry principles may potentially enable higher-order discrete rotational symmetry through directed template growth, arbitrary control over the azimuthal structure of a spherical particle displaying no symmetry is out of reach of current approaches. The in-fiber breakup strategy permits sophisticated yet facile and systematic azimuthal-symmetry engineering via core segmentation. Two examples of "beach ball" particles in Fig. 4—consisting of alternating segments of two different glasses G_1 and G_2—illustrate this unique capability: (*i*) a particle exemplifying discrete fourfold rotational symmetry by arranging G_1 and G_2 in equally sized quadrants (Fig. 4 *A*–*C*); and (*ii*) a particle with broken sixfold rotational symmetry by substituting one G_1-sextant with G_2 (Fig. 4 *D*–*F*). We compare the particle structures to that of the preform and fiber by optically imaging successive layers revealed within the particle through gradual polishing.

Combined Control over the Radial and Azimuthal Structure. The above-described procedures for radial and azimuthal structuring are independent and may thus be realized simultaneously in a single geometry. We highlight this unique capability by combining elements of radial and azimuthal engineering to produce core–shell particles (radial control) where each layer has a Janus structure (azimuthal control). Moreover, we control the relative orientation of the two broken-symmetry layers with respect to each other. The resulting particle thus comprises four materials carefully compartmentalized within the 3D volume of the particle as confirmed by combined structural and compositional imaging (Fig. 5 *A*–*D*). Another example

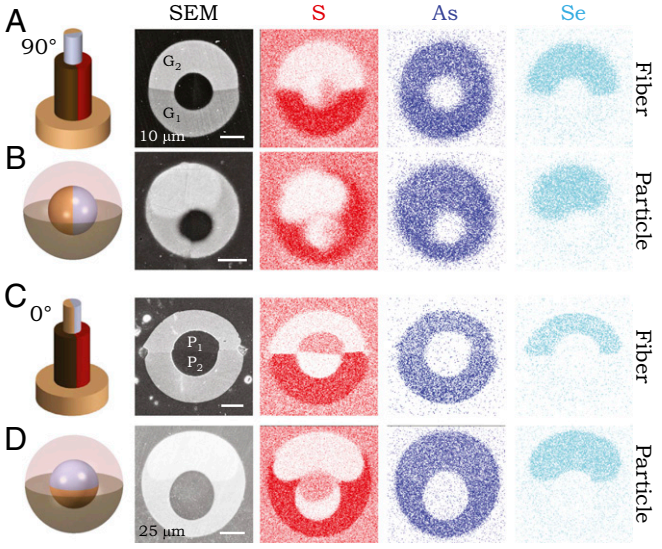

Fig. 5. Combined radial and azimuthal control over a particle's internal architecture. (*A*) A double-Janus particle: a core and shell each consisting of two halves of different materials. Here, the two symmetry-breaking axes are orthogonal. From *Left* to *Right*: A schematic of the fiber structure, SEM micrograph of the fiber cross-section, and energy-dispersive X-ray spectroscopy micrographs identifying the elements S, As, and Se. (*B*) Same as *A*, except the cross-sections are midplane through a particle resulting from the breakup of the fiber in *A*. (*C* and *D*) Same as *A* and *B*, except the symmetry-breaking axes in the core and shell are parallel. G_1, As_2S_3; G_2, $Ge_{1.3}(As_2Se_3)_{98.7}$; P_1, PES; P_2, PEI.

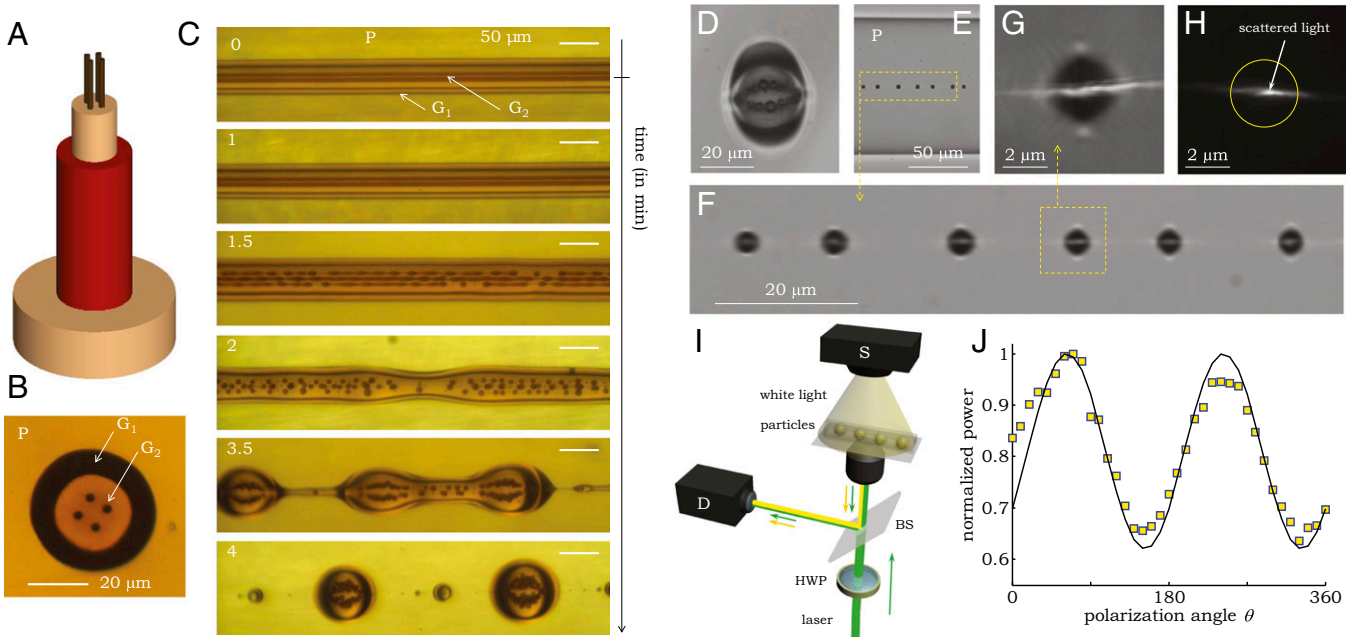

Fig. 6. Broken azimuthal symmetry in a spherical particle enables polarization-sensitive scattering. (*A*) Schematic of the fiber structure that produces strings of high-index contrast nanoparticles within a photonic particle. (*B*) Optical transmission micrograph of the fiber cross-section. (*C*) Optical transmission micrographs capturing the fiber breakup dynamics during thermal treatment. First, the four G_2 [$Ge_{1.3}(As_2Se_3)_{98.7}$] inner threads break up in parallel strings of smaller particles, and then the polymer cladding P (PES) and thin glass shell G_1 (As_2S_3) subsequently break up. Time is indicated in the *Top Left* corner of each panel. (*D*) Optical transmission micrograph through a microparticle produced in *C*. (*E*) Transmission optical micrograph of a section of fiber containing a necklace of 3-μm–diameter particles with the same structure as in *D*. (*F*) Higher-magnification micrograph of a section of the fiber in *E*. White light is used in imaging, whereas a green laser is imaged in reflection (the horizontal white line) and scatters strongly parallel to the axis along which the internal high-index nanoparticles are aligned. (*G*) A micrograph of a single particle from *F* with combined laser and white-light scattering. (*H*) Micrograph of laser light scattering from a single particle (white light turned off). The yellow circle is a guide to the eye and corresponds to the particle surface. (*I*) Schematic depiction of the optical arrangement for measuring the polarization-dependent scattering. The yellow beam indicates the transmitted white light used to align the sample, whereas the green one corresponds to the laser radiation used to measure the backscattering. HWP, half-wave plate; BS, beam splitter; S, source; D, detector. (*J*) Sinusoidal modulation of the integrated scattered intensity (squares) as a function of incident polarization angle. The maximum occurs when light is polarized along the direction of the internal nanoparticle strings. Squares are the data, and the solid line is a sinusoidal fit.

of combined radial and azimuthal structural control in a trimaterial particle (two glasses and one polymer) is shown in Fig. 6 in which four thin high-index glass threads are embedded in a low-index polymer surrounded by a high-index thin glass shell. The disparity between the diameters of the glass threads and the polymer results in the threads first breaking up into four parallel strings of smaller particles followed by breakup of the polymer into spherical particles containing the smaller glass particles. Movie S2 shows the real-time breakup dynamics of this fiber, whereas Movie S3 shows the internal particle structure obtained by 3D confocal optical microscopy. Such a multimaterial particle has broken spherical symmetry with a preferred optical axis along the particle strings.

Polarization-Dependent Optical Scattering. Azimuthal structural engineering of a particle can enable controlling the polarization of electromagnetic waves. In particular, a spherical photonic particle with broken internal azimuthal symmetry of sufficiently high refractive-index contrast exhibits polarization-dependent scattering. When a plane wave illuminates a spherical particle whose diameter is much smaller than the wavelength, there is no phase shift between the electric fields components polarized parallel and perpendicular to the scattering plane. We designed the internal structure of the particles in Fig. 6 *A*–*C* such that the four lines of high refractive-index small nanoparticles inside each particle (Fig. 6 *D*–*F*) break its azimuthal symmetry by scattering light in a similar fashion to finite cylinders (Fig. 6 *G* and *H*). We demonstrate polarization-dependent scattering from these structured particles using the arrangement shown in Fig. 6*I*, where linearly polarized monochromatic light is focused on a single particle and backscattered light is collected in reflection mode while the incident polarization is rotated (*Methods*). We observe significantly stronger scattering when the incident polarization is aligned parallel to the internal lines of nanoparticles with respect to the orthogonal polarization (Fig. 6*J*).

Discussion

The desire to impart form to matter has driven much of our technological mastery over nature. We have shown here that such control can be extended to the internal architecture of spherical multimaterial photonic particles—ones at the scale of an optical wavelength combining multiple high-index contrast materials. By exploiting an in-fiber fluid instability, multiple materials—including polymers and glasses—are compartmentalized at designated radial and azimuthal positions in the coordinate system of the particle. The critical feature that distinguishes our approach is that the structure is encoded at a macroscopic scale in the preform and the characteristic length scale is then translated down across orders of magnitude via thermal drawing (35). Furthermore, the relative orientation of the azimuthal structures in each radial layer may be varied—a feature unique to our fabrication strategy and currently inaccessible to other approaches. The process is efficient, scalable, in principle scale-free, and only minimal modifications to the procedure are required to change the target particle architecture, thereby enabling the digital design of photonic particles endowed with unprecedentedly sophisticated structures, which have implications for introducing new optical scattering capabilities without changing the particle size or materials selection.

A future road map emerges: starting from a desired far-field or near-field optical scattering phase function for a single

particle, what is the particle structure (the internal 3D refractive-index distribution) that is required? This inverse optical problem has not yet been solved in its entirety (50, 51). Furthermore, although we have exercised here control over the real part of the refractive index of the internal architecture of a photonic particle, it is possible to extend this approach to other physical attributes, such as the imaginary part of the refractive index (corresponding to optical gain or loss according to its sign). Gain may be imparted by doping a polymeric section of the particle with a fluorescent dye or with quantum dots, which may lead to particles satisfying the conditions for so-called PT symmetry and other non-Hermitian photonic structures (52). Moreover, non-optical physical attributes of the particles, such as the direction of their thermal emissivity (53), may be controlled through multimaterial structural engineering.

Methods

Scattering-Strength Measurements. Particles are extracted by dissolving the polymer cladding using dimethylacetamide at room temperature and are then deposited on a coverslip that is placed on the prism. The intensity distributions were measured across a 10 × 10-μm^2 plane situated at a height ≈2 μm above the particle using a Nanonics MultiView 4000 tuning-fork near-field scanning optical microscope in standard collection mode. Scattered light is collected using a Cr-Au–coated tapered silica fiber probe (Nanonics) with 50-nm–diameter aperture connected to a photon multiplying tube (Hamamatsu; H7421). See *SI Appendix, S5.1: Scattering-Strength Measurements*, for further details.

Polarization Measurements. The particles are retained in the fiber without removing the cladding such that they all have the same orientation with respect to the fiber axis. The sample is first illuminated with white light to identify and align the particle (Fig. 6 *E* and *F*), and then with a green linearly polarized laser (532-nm wavelength) focused at approximately midplane of the particle. Images are recorded using a Nikon Eclipse Ti microscope. With the white light turned off, we imaged the scattered green light across a single particle (Fig. 6*H*) and evaluate the integrated scattered intensity as a function of incident polarization. See *SI Appendix, S5.3: Polarization Measurements*, for further details.

ACKNOWLEDGMENTS. We thank D. S. Deng and S. J. Johnson for useful discussions, and S. Dai, X. Wang, H. Ren, and K. Yan for assistance. This work was funded by National Science Foundation Award CMMI-1002295, Air Force Office of Scientific Research (AFOSR) Contract FA-9550-12-1-0148, and AFOSR MURI Contract FA9550-14-1-0037, and in part by the Massachusetts Institute of Technology Materials Research Science and Engineering Center (MRSEC) through the MRSEC Program of the National Science Foundation under Award DMR-1419807.

1. Qiu C, Gao L, Joannopoulos JD, Soljačić M (2010) Light scattering from anisotropic particles: Propagation, localization, and nonlinearity. *Laser Photonics Rev* 4(2): 268–282.
2. Luk'yanchuk B, Miroshnichenko A, Kivshar YS (2013) Fano resonances and topological optics: An interplay of far-and near-field interference phenomena. *J Opt* 15(7):073001.
3. Cho EC, Glaus C, Chen J, Welch MJ, Xia Y (2010) Inorganic nanoparticle-based contrast agents for molecular imaging. *Trends Mol Med* 16(12):561–573.
4. Bai MY, et al. (2012) A facile and general method for the encapsulation of different types of imaging contrast agents within micrometer-sized polymer beads. *Adv Funct Mater* 22(4):764–770.
5. Kircher MF, et al. (2012) A brain tumor molecular imaging strategy using a new triple-modality MRI-photoacoustic-Raman nanoparticle. *Nat Med* 18(5):829–834.
6. Hottel H, Sarofim A, Dalzell W, Vasalos I (1971) Optical properties of coatings. Effect of pigment concentration. *AIAA J* 9(10):1895–1898.
7. Levinson R, Berdahl P, Akbari H (2005) Solar spectral optical properties of pigments—Part I: Model for deriving scattering and absorption coefficients from transmittance and reflectance measurements. *Sol Energy Mater Sol Cells* 89(4):319–349.
8. Levinson R, Berdahl P, Akbari H (2005) Solar spectral optical properties of pigments—Part II: Survey of common colorants. *Sol Energy Mater Sol Cells* 89(4):351–389.
9. Lambourne R, Strivens TA (1999) *Paint and Surface Coatings: Theory and Practice* (Woodhead Publishing, Cambridge, UK).
10. Fialkowski M, Bitner A, Grzybowski BA (2005) Self-assembly of polymeric microspheres of complex internal structures. *Nat Mater* 4(1):93–97.
11. Utada AS, et al. (2005) Monodisperse double emulsions generated from a microcapillary device. *Science* 308(5721):537–541.
12. Perry JL, Herlihy KP, Napier ME, Desimone JM (2011) PRINT: A novel platform toward shape and size specific nanoparticle theranostics. *Acc Chem Res* 44(10):990–998.
13. Lee H, Kim J, Kim H, Kim J, Kwon S (2010) Colour-barcoded magnetic microparticles for multiplexed bioassays. *Nat Mater* 9(9):745–749.
14. Lee J, et al. (2014) Universal process-inert encoding architecture for polymer microparticles. *Nat Mater* 13(5):524–529.
15. Tribelsky MI, Geffrin J-M, Litman A, Eyraud C, Moreno F (2015) Small dielectric spheres with high refractive index as new multifunctional elements for optical devices. *Sci Rep* 5:12288.
16. Person S, et al. (2013) Demonstration of zero optical backscattering from single nanoparticles. *Nano Lett* 13(4):1806–1809.
17. Liu W, Miroshnichenko AE, Neshev DN, Kivshar YS (2012) Broadband unidirectional scattering by magneto-electric core-shell nanoparticles. *ACS Nano* 6(6):5489–5497.
18. Fu YH, Kuznetsov AI, Miroshnichenko AE, Yu YF, Luk'yanchuk B (2013) Directional visible light scattering by silicon nanoparticles. *Nat Commun* 4:1527.
19. Tsuchimoto Y, et al. (2015) Controlling the visible electromagnetic resonances of Si/SiO_2 dielectric core–shell nanoparticles by thermal oxidation. *Small* 11(37):4844–4849.
20. Li Y, et al. (2015) Broadband zero-backward and near-zero-forward scattering by metallo-dielectric core-shell nanoparticles. *Sci Rep* 5:12491.
21. Staude I, et al. (2013) Tailoring directional scattering through magnetic and electric resonances in subwavelength silicon nanodisks. *ACS Nano* 7(9):7824–7832.
22. Sautter J, et al. (2015) Active tuning of all-dielectric metasurfaces. *ACS Nano* 9(4): 4308–4315.
23. Decker M, et al. (2015) High-efficiency dielectric Huygens' surfaces. *Adv Opt Mater* 3(6):813–820.
24. Wu C, et al. (2014) Spectrally selective chiral silicon metasurfaces based on infrared Fano resonances. *Nat Commun* 5:3892.
25. Li Y, et al. (2015) On-chip zero-index metamaterials. *Nat Photonics* 9(11):738–742.
26. Shabahang S, Kaufman J, Deng D, Abouraddy A (2011) Observation of the Plateau-Rayleigh capillary instability in multi-material optical fibers. *Appl Phys Lett* 99(16):161909.
27. Kaufman JJ, et al. (2012) Structured spheres generated by an in-fibre fluid instability. *Nature* 487(7408):463–467.
28. Kaufman JJ, et al. (2013) In-fiber production of polymeric particles for biosensing and encapsulation. *Proc Natl Acad Sci USA* 110(39):15549–15554.
29. Abouraddy AF, et al. (2007) Towards multimaterial multifunctional fibres that see, hear, sense and communicate. *Nat Mater* 6(5):336–347.
30. Tao G, Stolyarov AM, Abouraddy AF (2012) Multimaterial fibers. *Int J Appl Glass Sci* 3(4):349–368.
31. Tao G, et al. (2015) Infrared fibers. *Adv Opt Photonics* 7(2):379–458.
32. Rayleigh L (1879) On the capillary phenomena of jets. *Proc R Soc Lond* 29(196–199):71–97.
33. Eggers J, Villermaux E (2008) Physics of liquid jets. *Rep Prog Phys* 71(3):036601.
34. Tao G, Shabahang S, Banaei E-H, Kaufman JJ, Abouraddy AF (2012) Multimaterial preform coextrusion for robust chalcogenide optical fibers and tapers. *Opt Lett* 37(13):2751–2753.
35. Kaufman JJ, et al. (2011) Thermal drawing of high-density macroscopic arrays of well-ordered sub-5-nm-diameter nanowires. *Nano Lett* 11(11):4768–4773.
36. Khudiyev T, Tobail O, Bayindir M (2014) Tailoring self-organized nanostructured morphologies in kilometer-long polymer fiber. *Sci Rep* 4:4864.
37. Aktas O, et al. (2014) A new route for fabricating on-chip chalcogenide microcavity resonator arrays. *Adv Opt Mater* 2(7):618–625.
38. Gumennik A, et al. (2013) Silicon-in-silica spheres via axial thermal gradient in-fibre capillary instabilities. *Nat Commun* 4:2216.
39. Tomotika S (1935) On the instability of a cylindrical thread of a viscous liquid surrounded by another viscous fluid. *Proc R Soc Lond A Math Phys Sci* 150(870):322–337.
40. Liang X, Deng D, Nave J-C, Johnson SG (2011) Linear stability analysis of capillary instabilities for concentric cylindrical shells. *J Fluid Mech* 683:235–262.
41. Bohren CF, Huffman DR (1983) *Absorption and Scattering of Light by Small Particles* (Wiley, New York).
42. Bass M, et al. (2009) *Handbook of Optics, Volume IV: Optical Properties of Materials* (McGraw-Hill, New York), 3rd Ed.
43. Chew H, Wang D-S, Kerker M (1979) Elastic scattering of evanescent electromagnetic waves. *Appl Opt* 18(15):2679–2687.
44. Liu C, Kaiser T, Lange S, Schweiger G (1995) Structural resonances in a dielectric sphere illuminated by an evanescent wave. *Opt Commun* 117(5):521–531.
45. Barchiesi D, Van Labeke D (1993) Application of Mie scattering of evanescent waves to scanning tunnelling optical microscopy theory. *J Mod Opt* 40(7):1239–1254.
46. Bekshaev AY, Bliokh KY, Nori F (2013) Mie scattering and optical forces from evanescent fields: A complex-angle approach. *Opt Express* 21(6):7082–7095.
47. Glotzer SC, Solomon MJ (2007) Anisotropy of building blocks and their assembly into complex structures. *Nat Mater* 6(8):557–562.
48. Yan J, Bloom M, Bae SC, Luijten E, Granick S (2012) Linking synchronization to self-assembly using magnetic Janus colloids. *Nature* 491(7425):578–581.
49. Walther A, Müller AH (2013) Janus particles: Synthesis, self-assembly, physical properties, and applications. *Chem Rev* 113(7):5194–5261.
50. Naraghi RR, Sukhov S, Dogariu A (2015) Directional control of scattering by all-dielectric core-shell spheres. *Opt Lett* 40(4):585–588.
51. Hsu CW, DeLacy BG, Johnson SG, Joannopoulos JD, Soljačić M (2014) Theoretical criteria for scattering dark states in nanostructured particles. *Nano Lett* 14(5):2783–2788.
52. El-Ganainy R, Makris KG, Christodoulides DN, Musslimani ZH (2007) Theory of coupled optical PT-symmetric structures. *Opt Lett* 32(17):2632–2634.
53. Jin W, Polimeridis AG, Rodriguez AW (2015) Temperature control of thermal radiation from heterogeneous bodies. arXiv:1507.00265.

Supporting Information

Tao et al. 10.1073/pnas.1601777113

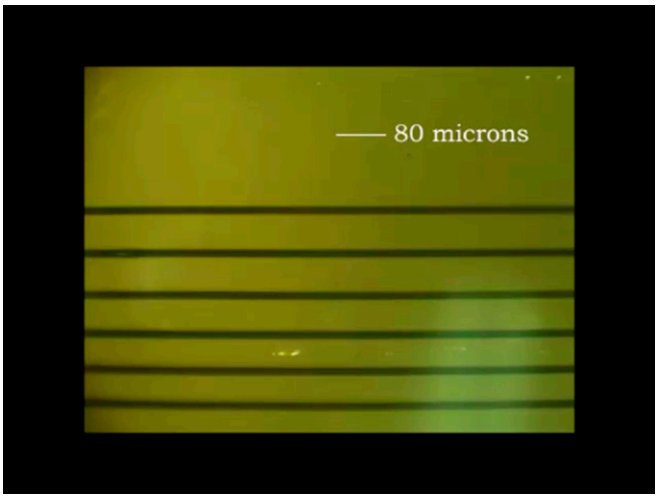

Movie S1. A movie in real time of the breakup of six parallel cores embedded in a fiber during heating. The sample is a 2-cm-long PES polymer fiber with a rectangular cross-section (0.3×1 mm^2) containing six equally spaced G_2 cores, each 20 μm in diameter and separated by 100 μm from its nearest neighbor. A rectangular—rather than a cylindrical—fiber was used to eliminate optical lensing effects resulting from a curved outer surface and to reduce the fiber movement or disturbance during thermal processing.

Movie S1

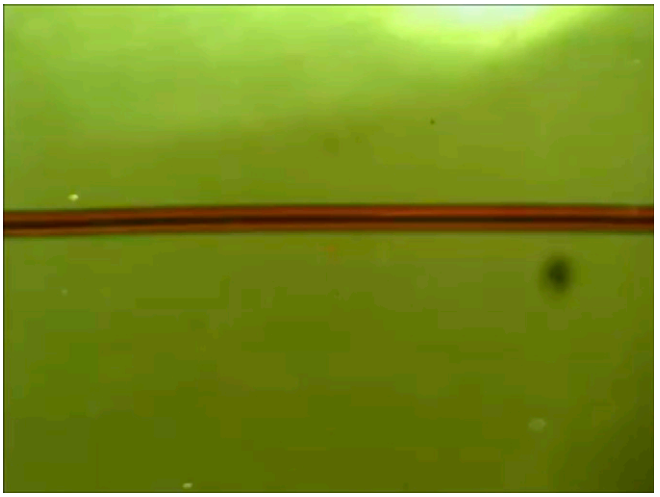

Movie S2. A movie in real time of the breakup during heating of the fiber shown in Fig. 6*A* of the main text (cross-section shown in Fig. 6*B* and side view in Fig. 6*C*). The core consists of a thin glass G_1 shell enveloping a PES core containing four parallel G_2 filaments. The diameter of this structure is ~40 μm. Because of their smaller diameter, the four G_2 filaments undergo the breakup process first, resulting in four lines of smaller particles. Subsequently, breakup takes place in the outer G_1 shell, resulting in large-diameter particles containing the smaller particles aligned along the axis.

Movie S2

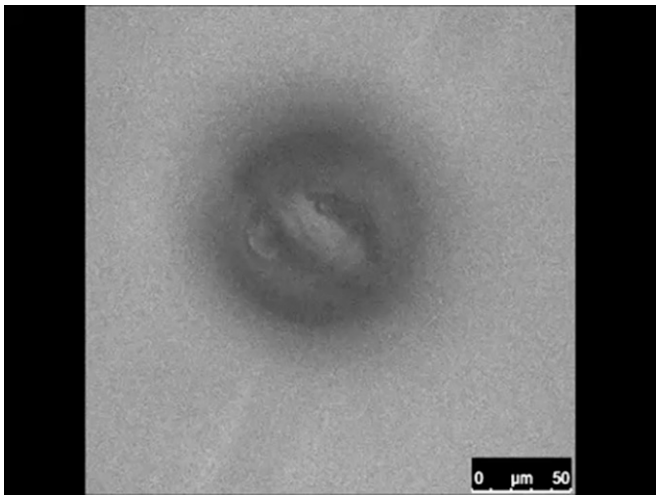

Movie S3. A movie displaying a sequence of imaged planes through a single structured particle (Fig. 6 in the main text; Movie S2) captured by an optical confocal microscope. The different planes stepping through the particle reveal the four lines of the smaller-sized G_2 particles aligned along the axis contained embedded in a polymer within the larger particle, which is enclosed in an outer G_1 shell.

Movie S3

Other Supporting Information Files

SI Appendix (PDF)

Digital design of multimaterial photonic particles

Guangming Tao,[1] Joshua J. Kaufman,[1] Soroush Shabahang,[1] Roxana R. Naraghi,[1,2] Sergey V. Sukhov,[1] John D. Joannopoulos,[3] Yoel Fink,[3] Aristide Dogariu,[1] and Ayman F. Abouraddy[1†]

[1]*CREOL, The College of Optics & Photonics, University of Central Florida, Orlando, FL 32816 USA*

[2]*Department of Physics, University of Central Florida, Orlando, FL 32816 USA*

[3]*Research Laboratory of Electronics, Massachusetts Institute of Technology, Cambridge, Massachusetts 02139, USA*

[†] Corresponding author. Email: raddy@creol.ucf.edu

Supplementary Information Appendix

Table of contents

S1. Overview of the preform preparation process

S2. Structured-preform fabrication

S2.1 Preform for core-shell particles

S2.2 Preform for multi-shell particles

S2.3 Preform for azimuthally structured particles with discrete rotational symmetry

S2.4 Preform for azimuthally structured particles with broken azimuthal symmetry

S2.5 Preform for double-Janus particles

S2.6 Preform for multi-core particles

S3. Capturing the in-fiber particle formation via the PRI

S4. Dependence of the breakup dynamics on the core-shell diameter

S5. Experimental details

S5.1 Scattering-strength measurements

S5.2 Theory for modeling evanescent excitation

S5.3 Polarization measurements

S1. Overview of the preform preparation process

We provide in this Supplementary Information document the details of the processes implemented for preform preparation and fiber drawing. The resulting fibers were then used to produce the digitally designed particles studied in our paper via an in-fiber Plateau-Rayleigh capillary instability (PRI).

The fibers used in this study were all fabricated by thermal drawing from a macroscopic scaled-up model called a 'preform' – the standard approach used in producing telecommunications fibers. A preform has the same cross-sectional geometry of the target fiber, albeit with significantly larger transverse feature dimensions. The preforms were all thermally drawn in the viscous state in a home-built fiber draw tower at CREOL, The College of Optics & Photonics, University of Central Florida. The transverse dimensions of the preform are reduced during the draw concomitantly with axial extension, resulting in hundreds of meters of fibers with complex cross-sectional architecture. Although the structured preforms used in producing the digitally designed multimaterial photonic particles described in the text all differ in geometry and material composition, nevertheless, the *overall process* of fiber drawing from a preform was the same in all cases.

The structured preforms are prepared by combining several standard macroscopic processing techniques such as melt-casting, extrusion, machining, thin-film rolling, stack-and-draw, etc. The details of the fabrication steps followed in preparing each preform are presented in Section S2. For more details about these general technologies in application to fiber-preform preparation, see Ref. [S1]. Indeed, the possibility of combining simple, readily accessible processing techniques harnessed for fiber-preform fabrication provides the underpinning for the wide potential for digitally designing complex multimaterial photonic particles.

For each preform, the outer diameter is adjusted by rolling additional thin polymer films followed by thermal consolidation under vacuum. The fibers must be drawn such that the diameter of the fiber core is on the order of that of the desired particle diameter. The draw-down ratio (the ratio of the preform-to-fiber diameters) should be in the range of 10 – 40 to obtain a uniform fiber in a stable manner. Therefore, to reduce the core diameter in the initial preform (typically on the order of several millimeters) to the micrometer scale, we rely on multiple thermal drawing steps in which the core diameter is reduced recursively. A section (or multiple sections) of a drawn fiber

is incorporated into a polymer preform, which is in turn thermally drawn into a fiber. Using this so-called 'stack-and-draw' approach, one may reach a core diameter of 5 nm starting from a rod of diameter 10 mm [S2].

We present below an outline of the general steps for fiber drawing exemplified with a simple glass-core/polymer-cladding fiber (Fig. 2e in the main text). Three main steps are required: (1) materials synthesis and preparation, (2) preform construction and consolidation, and (3) fiber drawing. The more complex preforms are described in Section S2.

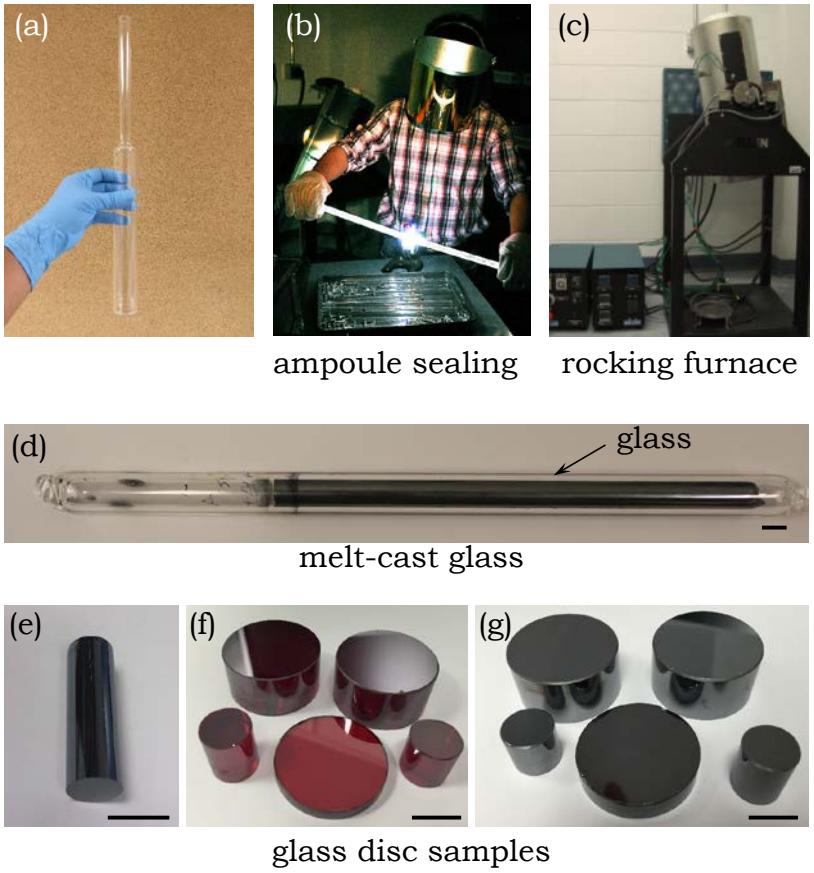

Figure S1 | Overall approach for chalcogenide glass preparation. (a) Silica ampoules for glass melt-casting. (b) A propane-oxygen torch flame is used for sealing a silica ampoule containing the chalcogenide glass. (c) A rocking furnace (The Mellen Company) is used for melt-casting a glass rod. (d) A sealed silica ampoule containing the melt-cast chalcogenide glass. (e)-(g) Examples of chalcogenide glass discs and rods of different sizes: (e) $Ge_{1.3}(As_2Se_3)_{98.7}$, (f) As_2S_3, and (g) As_2Se_3. The scale bars in (d)-(g) are 10 mm.

Glass preparation. Two inorganic non-oxide chalcogenide glasses (G_1: $As_{40}S_{60}$ and G_2: $Ge_{1.3}As_{39.48}Se_{59.22}$) are used in our work. Both glasses are prepared in the form of rods utilizing the melt-quenching technique [S3]. The glass rods are typically 30-mm-long and are prepared in three diameter sizes: 30 mm, 12 mm, and 10 mm. Commercial glass materials (AMTIR-2: $As_{40}Se_{60}$ and AMTIR-6: $As_{40}S_{60}$; Amorphous Materials, Inc.) were crushed into small pieces (~ 3 mm in size) and loaded into silica ampoules having the target diameter. In the case of G_2, high-purity Ge (Alfa Aesar) was introduced into $As_{40}Se_{60}$ to reach the desired composition, which was selected since it has approximately similar viscosity to G_1 at the particle breakup temperature (~ 350 – 400 °C) [S4]. The ampoules are sealed using a propane-oxygen torch at a vacuum pressure of 10^{-4} Pa. After melting in a rocking furnace at 900 – 950 °C for 12 hours, the glass samples are quenched in cold water and annealed near their glass transition temperature to reduce inner stresses [S5]. The annealed glass is removed from the ampoule and sectioned into 30-mm-long rods. See Fig. S1 for an outline of the process.

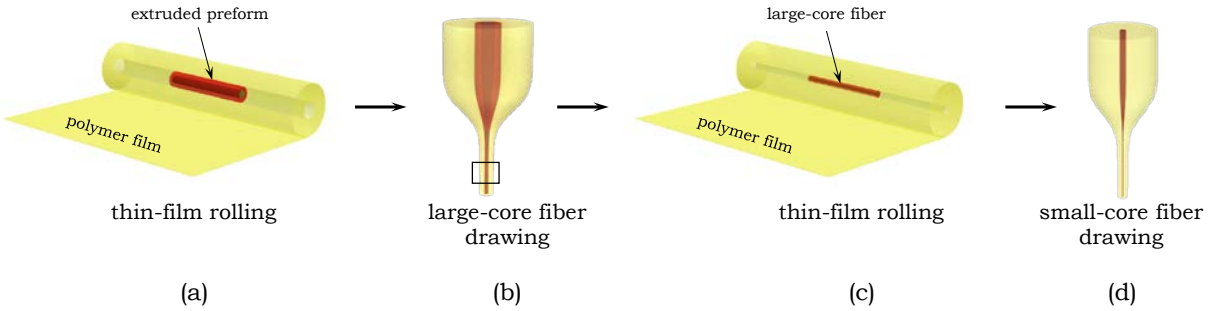

Figure S2 | Overall approach for thermally drawing multimaterial fibers to produce structured spherical particles via an in-fiber fluid instability. (a) Structured fiber preform preparation by rolling a thin polymer film around an extruded, structured preform (shown here as a two-layer rod). (b) The consolidated preform is then thermally drawn into an extended fiber. (c) A section of the drawn fiber in (b) is subsequently used in the same polymer-film-rolling procedure as in (a) to create a new preform. (d) The preform from (c) is consolidated and thermally drawn, thus further reducing the core diameter.

Preform preparation. The preforms were in the most part prepared by multimaterial one-step coextrusion [S5-S7], as described in Section S2 below. The diameter of the extruded

rod is typically several millimeters. In addition to extrusion, we employ stack-and-draw and thin-film rolling techniques [S1, S8, S9]. These processes combined enable the fabrication of a wide range of complex structures. We typically roll a thin polymer film around the preform – followed by thermal consolidation under vacuum – to reach a standard diameter of 30 mm in preparation for thermal fiber drawing (Fig. S2a).

***Fiber drawing*.** A section of the preform (typical outer diameter is several millimeters and length is tens of millimeters) is rolled with a thin polymer film and is then thermally consolidated under vacuum to produce a preform typically with 25 – 35 mm outer diameter and 80 – 120 mm length (Fig. S2a). The preform is thermally drawn continuously into an extended fiber typically with an outer diameter of 1 mm. At this stage, the core is a few-hundred microns in diameter (Fig. S2b). A section of this large-core fiber (typical length 80 – 100 mm) is subsequently rolled with more polymer film to form a second preform (Fig. S2c) with similar dimensions to that of the initial one (Fig. S2a). The preform – after consolidation – is thermally drawn into a fiber that now has a small-core diameter (typical diameter is tens of microns). By repeating this process, the core diameter – and thus the diameter of the particles produced via the PRI – can be reduced by orders of magnitude with respect to the initial diameter [S2].

S2. Structured-preform fabricated

S2.1 Preform for core-shell particles

To refer to the various multilayer fibers and particles described in the main text (Fig. 2), we adopt the following notation. The outermost cladding in all cases is a polymer (P) while the multilayered core structure varies. We refer to each fiber by a sequence of layers starting from the core towards the outer cladding. For example, the simple glass-core/polymer-cladding fiber described in Section S1 is denoted G**P**. We used a bold font for **P** to identify that this is the outer sacrificial cladding that will not be included in the resulting photonic particles harvested from the fibers after inducing the PRI. In the case of the core-shell particles, where the core is a polymer and the shell is a glass, the structure is referred to as PG**P**.

The PG**P** preform drawn into the core-shell fiber shown in Fig. 2f of the main text was produced by extruding the vertically stacked billet shown in Fig. S3a using one-step multimaterial stacked coextrusion [S1, S6]. Three 30-mm-diameter discs are stacked vertically atop of each other in the billet: polyethersulfone (PES) polymer on the top, followed by G_1, and then PES at the bottom with heights 30, 20, and 20 mm, respectively. The stacked billet is extruded through a 6-mm-diameter circular die at a temperature close to material softening temperature with a force ~ 800 lb.

Multimaterial stacked coextrusion produces a cylindrically nested multilayer preform, but with a tapered internal structure along its axis [S5]; Fig. S3d. A section of the extruded rod is selected (outer diameter = 6 mm, glass-shell inner diameter = 3.2 mm) and is used to prepare a preform for fiber drawing, followed by thin-film-rolling with a 125-μm-thick PES film (Ajedium) and thermal consolidation under vacuum to increase the outer diameter to 30 mm (Fig. S2a). The consolidated preform is thermally drawn into a 2-mm-diameter fiber containing a 213-μm-diameter glass shell; Fig. S2b. A section of this fiber is further rolled with 125-μm-thick PES film to 21.3-mm-outer-diamter, followed by thermal drawing into a 1-mm-diameter fiber with 10-μm-diameter glass shell. Fibers with different polymer-core to glass-shell ratios – resulting from different sections along the extruded preform (Fig. S3d) – were prepared in the range 0.2 to 0.8.

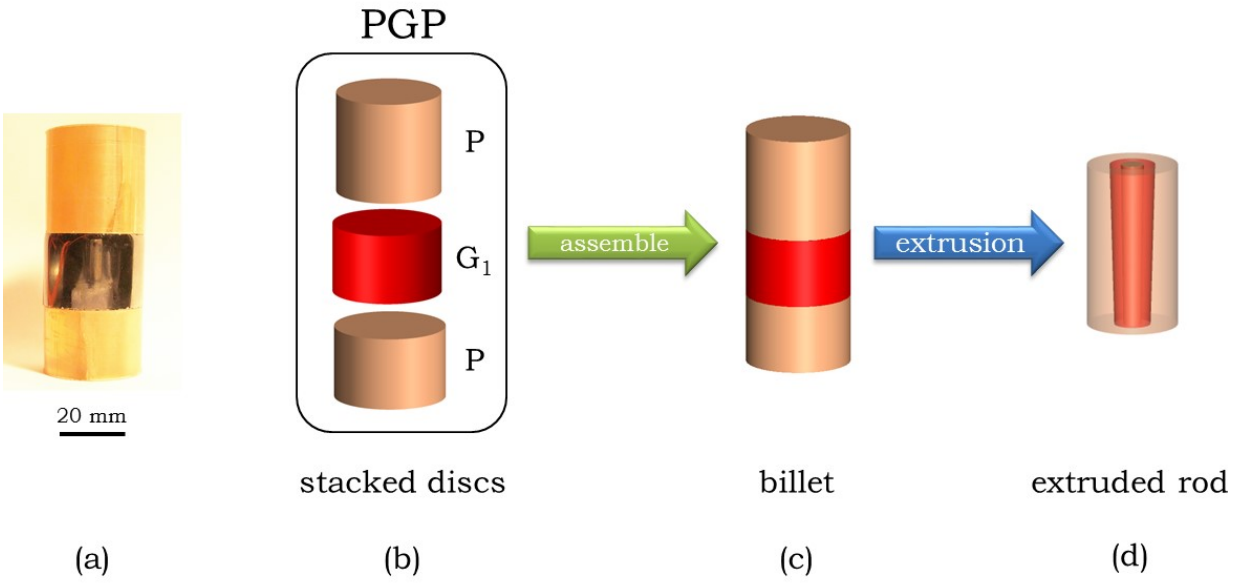

Figure S3 | Preparation of a preform for the core-shell fiber. (a) Photograph of the billet used consisting of a sequence of three stacked discs; from top to bottom: polymer, G_1, and polymer. (b) Three discs used to assemble the billet. P: polyethersulfone (PES). (c) The discs in (b) are assembled into an extrusion billet. (d) A section of an extruded cylindrical rod.

S2.2 Preform for multi-shell particles

Several techniques are combined in producing the preforms that led to the fabrication of three-layer and five-layer particles. We first outline the steps followed to produce the GPG**P** fiber (Fig. 2g in the main text) that yields three-layer particles after the thermally induced breakup.

(1) A 10-mm-diameter, 30-mm-long G_1 rod is prepared by melt-quenching (Section S1).

(2) A 125-μm-thick PES film was rolled around the rod to increase its outer diameter to 13.1 mm. Thermal consolidation under vacuum results in a GP assembly (Fig. S4a,b; top row).

(3) A thin-walled G_1 tube (inner diameter = 13.2 mm, outer diameter = 19.2 mm, length = 30 mm) is extruded from a 30-mm-diameter, 50-mm-long G_1 rod (Fig. S4a,b; bottom row). A 30-mm-long section of this extruded G_1 tube was sectioned.

(4) The GP assembly from step (2) is inserted into the thin-walled G_1 tube from step (3) to form a GPG structure (Fig. S4c; top).

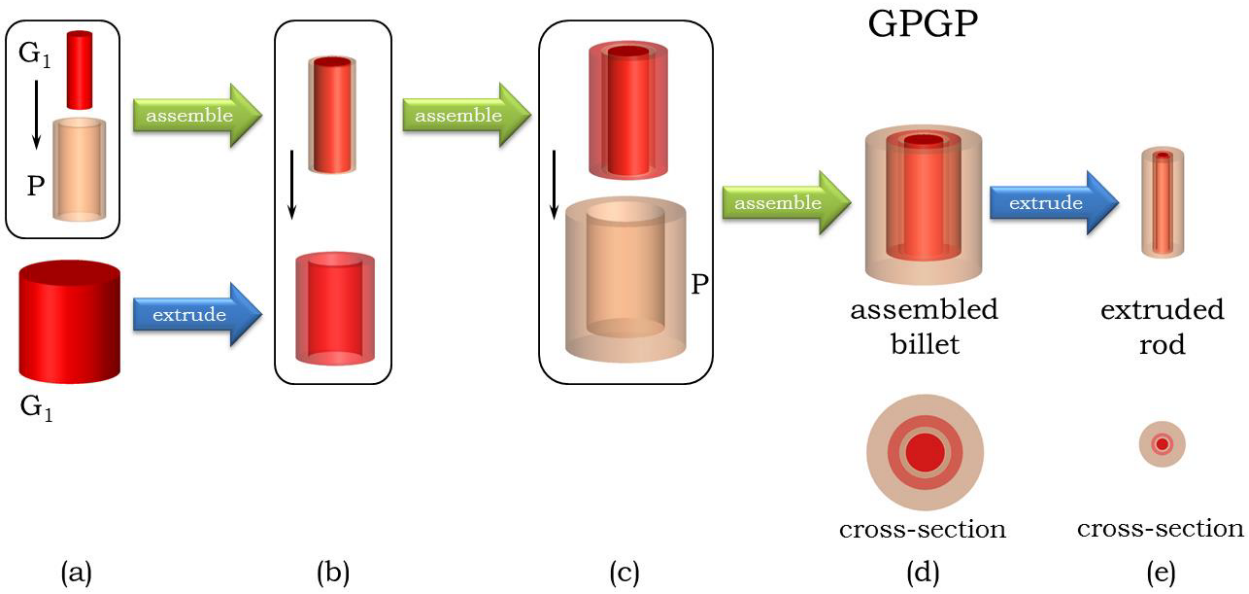

Figure S4 | Preparation of a preform for the three-layer fiber core. (a) A GP assembly and a G_1 rod (to be extruded into a tube) are prepared. (b) The GP assembly is inserted into an extruded glass tube to form a GPG assembly. (c) The GPG assembly is then placed inside a polymer rod with a stepped hole to form the GPG**P** billet assembly shown in (d). (e) The billet assembly is extruded into a cylindrical cane having the desired cross section, which is subsequently thermally drawn into an extended fiber.

(5) The GPG assembly is inserted into a 30-mm-diameter, 35-mm-long PES rod in which a 19.3-mm-diameter, 30-mm-deep stepped hole is drilled (Fig. S4c; bottom). The result is a GPG**P** assembly shown schematically in Fig. S4d, which constitutes an extrusion billet. Extrusion is necessary here to remove any gaps at the multilayer interfaces (details of the extrusion process can be found in Refs. [S6, S7, S10, S11]).

(6) The extruded GPG**P** cane has a sequence of layers with diameters (from the inside-out) of 2, 2.62, 3.84, and 6 mm. The ratios of these diameters is similar to those in the billet, except

that the dimensions are reduced and the gaps between the layers in the assembled billet are removed during extrusion (Fig. S4e).

(7) A segment of the extruded preform was sectioned and utilized in preparing a preform by thin-film-rolling followed by fiber drawing to produce GPG**P** fibers. This process was repeated twice to reduce the GPG core diameter to 20 μm, while encased in a polymer cladding of outer diameter 1 mm, ahead of particle breakup.

A similar sequence of steps was followed to produce a GPGPG**P** fiber (Fig. 2h in the main text) that yields five-layer particles after thermally induced breakup.

(1) A 10-mm-diameter, 30-mm-long G_1 rod is prepared by melt-quenching.

(2) This G_1 rod is rolled with a PES film to reach an outer diameter of 35.5 mm, resulting in a GP preform.

(3) A 3.55-mm-diameter cane was thermally drawn from this GP preform. A 30-mm-long segment of the cane was sectioned.

(4) A G_1 tube (inner diameter = 3.6 mm, outer diameter = 11.8 mm, length = 30 mm) is extruded from a 30-mm-diameter, 50-mm-long G_1 rod. A 30-mm-long segment of the G_1 tube was sectioned.

(5) The drawn GP cane from step (3) is inserted in the G_1 tube from step (4) to produce a GPG assembly.

(6) A thin-layer of PES film is rolled around the GPG assembly from step (5) to reach an outer diameter of 13.1 mm. A GPGP assembly is obtained.

(7) This GPGP assembly is inserted in a thin-wall G_1 tube (inner diameter = 13.2 mm, outer diameter = 19.2 mm, length = 30 mm) which is produced in step (3) of the procedure outlined above for producing in three-layer fibers. A GPGPG assembly is obtained.

(8) The GPGPG assembly from steps (1)-(7) is inserted into a 30-mm-diameter, 35-mm-long PES rod in which a 19.3-mm-diameter, 30-mm-deep stepped hole is drilled. The result is a GPGPG**P** assembly that constitutes an extrusion billet.

(9) The extruded GPGPG**P** cane has a sequence of layers with diameters (from the inside-out) of 0.32, 1.1, 3.67, 4.1, 6.0, and 9.4 mm.

(10) A segment of the extruded preform was sectioned and utilized in preparing a preform by thin-film-rolling followed by fiber drawing to produce GPGPG**P** fibers. This process was repeated twice to reduce the five-layer GPGPG core diameter to 42 μm, while encased in a polymer cladding of outer diameter is 1 mm, ahead of particle breakup.

S2.3 Preform for azimuthally structured particles with discrete rotational symmetry

Two pairs of 30-mm-long axisymmetric glass rods are prepared whose cross-sections are that of a quarter-circle (quadrants from 6-mm-radius circles). These rods were produced (Fig. S5a,b) by extruding 30-mm-diameter, 30-mm-long G_1 and G_2 cylinders through a die with appropriate aperture cross section. These two pairs of quarter-cylindrical glass rods were assembled by alternating from one glass to the other, such that the azimuthal cross-sectional structure sequence is G_1-G_2-G_1-G_2 (Fig. S5c).

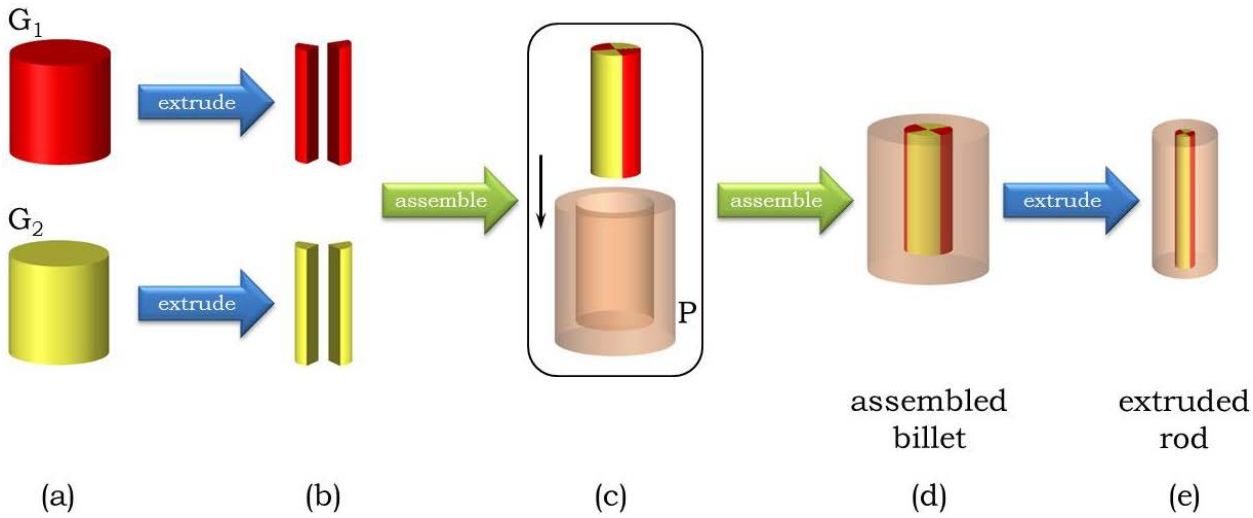

Figure S5 | Preparation of a preform for an azimuthally structured fiber with discrete rotational symmetry. (a) Two glass rods, G_1 and G_2, are prepared and (b) extruded into rods with quarter-circle cross sections. (c) Two pairs of glass segments from (b) are assembled into a cylindrical rod – constituting the core – with alternating G_1 and G_2 segments. The core is inserted into a stepped-hole polymer (P) rod to form the billet assembly in (d). (e) The billet in (d) is extruded into a cylindrical cane. See text for details.

This four-fold rotationally symmetric cylinder is inserted into a 30-mm-diameter, 35-mm-long PES rod in which a 12.1-mm-diameter, 30-mm-deep stepped hole is drilled. The resulting structure constitutes the extrusion billet (Fig. S5d). After extrusion, a solid structure with the same transverse structure of the assembly billet is produced, but with any gaps between the segments of the billet removed. A segment of the extruded cane (structured glass core diameter = 2.4 mm, outer diameter = 6 mm, length = 30 mm) is sectioned and a polymer (PES) thin film is rolled around it, followed by thermal consolidated under vacuum to produce a preform that is thermally drawn into a fiber. The process is repeated twice to reach the desired fiber dimensions; here the structured glass core diameter is 15 μm embedded in a 1-mm-diameter PES cladding in preparation for particle breakup (Fig. 4a-c in the main text).

S2.4 Preform for azimuthally structured particles with broken azimuthal symmetry

For the azimuthally *asymmetric* fiber, one half G_1 glass cylinder (radius = 6 mm; length = 30 mm), one 60° circular G_1 sector (radius = 6 mm; length = 30 mm) and two 60° circular G_2 sectors (radius = 6 mm; length = 30 mm) were produced by structured glass extrusion from large-scale G_1 and G_2 glass rods with 30-mm diameter and 30-mm height (Fig. S6a,b).

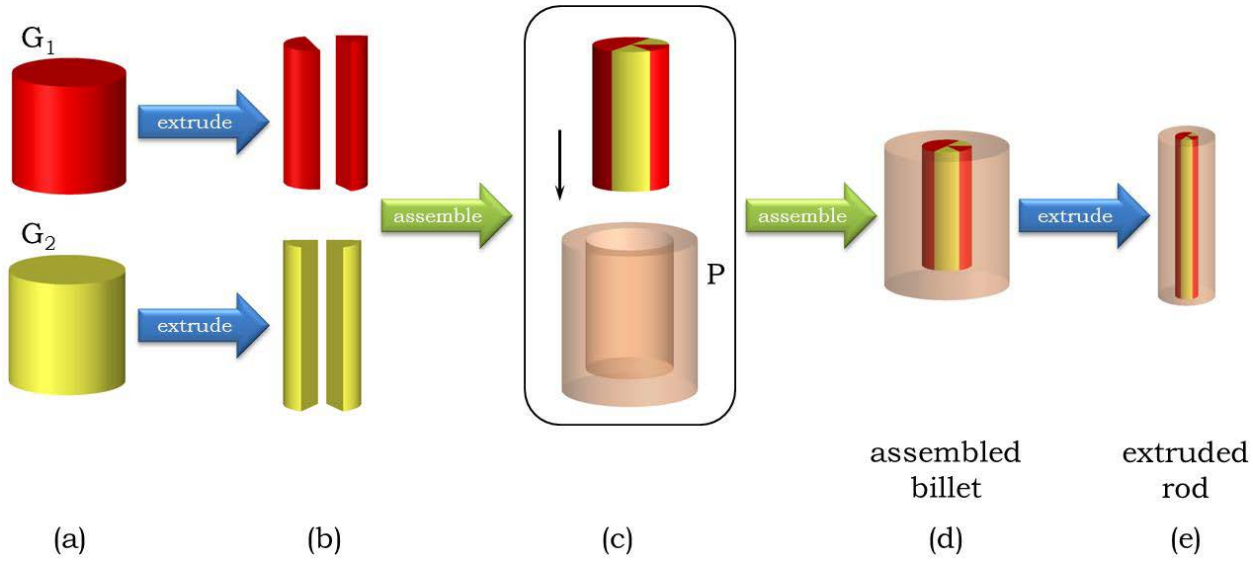

Figure S6 | Preparation of a preform for an azimuthally structured fiber with broken rotational symmetry. (a) Two glass rods, G_1 and G_2, are prepared and (b) extruded into

rods with 60°-circular-sector cross section for G_2, and both 60°-circular-sector and half-circle cross sections for G_1. (c) Glass rods from (b) are arranged into a cylindrical rod with alternating G_1 and G_2 segments in the geometry shown, constituting the core. The core is inserted into a stepped-hole polymer-rod, to form the billet assembly in (d). (e) The billet in (d) is extruded into a cylindrical cane. See text for details.

In a similar fashion to that employed in producing the structured preform with discrete rotational symmetry, four glass sections (Fig. S6b) are assembled into a glass cylinder with G_1-G_2-G_1-G_2 cross-sectional profile (Fig. S6c). The resulting rod – endowed with broken azimuthal symmetry – is inserted into a polymer rod with a suitably stepped hole (12.1-mm-diameter, 30-mm-deep in a 30-mm-diameter, 35-mm-high polymer rod), the composite rod is extruded into a 6-mm-diameter cane, followed by multiple thin-film rolling and thermal fiber drawing steps. The result is a fiber with the broken azimuthal symmetry (Fig. 4d-f in the main text) produced for particle breakup (core diameter = 15 μm, outer diameter = 1 mm).

S2.5 Preform for double-Janus particles

Two polymer (P_1: PES and P_2: PEI) rods and two glass (G_1 and G_2) rods with the same dimensions (diameter = 30 mm, height = 30 mm) are prepared by thin-film-rolling technique and melt-quenching technique, respectively (Fig. S7a). The polymer rods are extruded into half cylinders (radius = 6 mm, length = 30 mm), while the glass rods are extruded into half cylindrical tubes (inner radius = 6.1 mm, outer radius = 12 mm, length = 30 mm); Fig. S7b. The two polymer half cylinders are assembled into a Janus cylindrical rod, which – in turn – is placed inside a Janus tube formed by two glass half-cylindrical tubes (top row of Fig. S7c). As shown in Fig. S7, the interface between the two polymer halves is aligned with that of the glass assembly interface, a configuration we term a '0° double-Janus' structure. By rotating the relative position of the inner polymer rod assembly with respect to the outer glass tube assembly, we can produce a double-Janus structure with arbitrary relative orientation. In this work, we have produced 0° (Fig. 5c,d in the main text) and 90° (Fig. 5a,b in the main text) double-Janus fibers and particles. Similarly to the structured-fiber fabrication strategy previously described, this double-Janus assembly (top row of Fig. S7c) is inserted into a polymer rod with suitably stepped hole (12.1-mm-diameter, 30-mm-deep in a 30-

mm-diameter, 35-mm-high polymer rod), followed by extrusion (into a 6-mm-diameter cylindrical cane) and multiple thin-film-rolling and thermal-fiber-drawing steps. The resulting fiber (core diameter = 50 µm, outer diameter = 1 mm) was then used to produced particles via the PRI-driven breakup process.

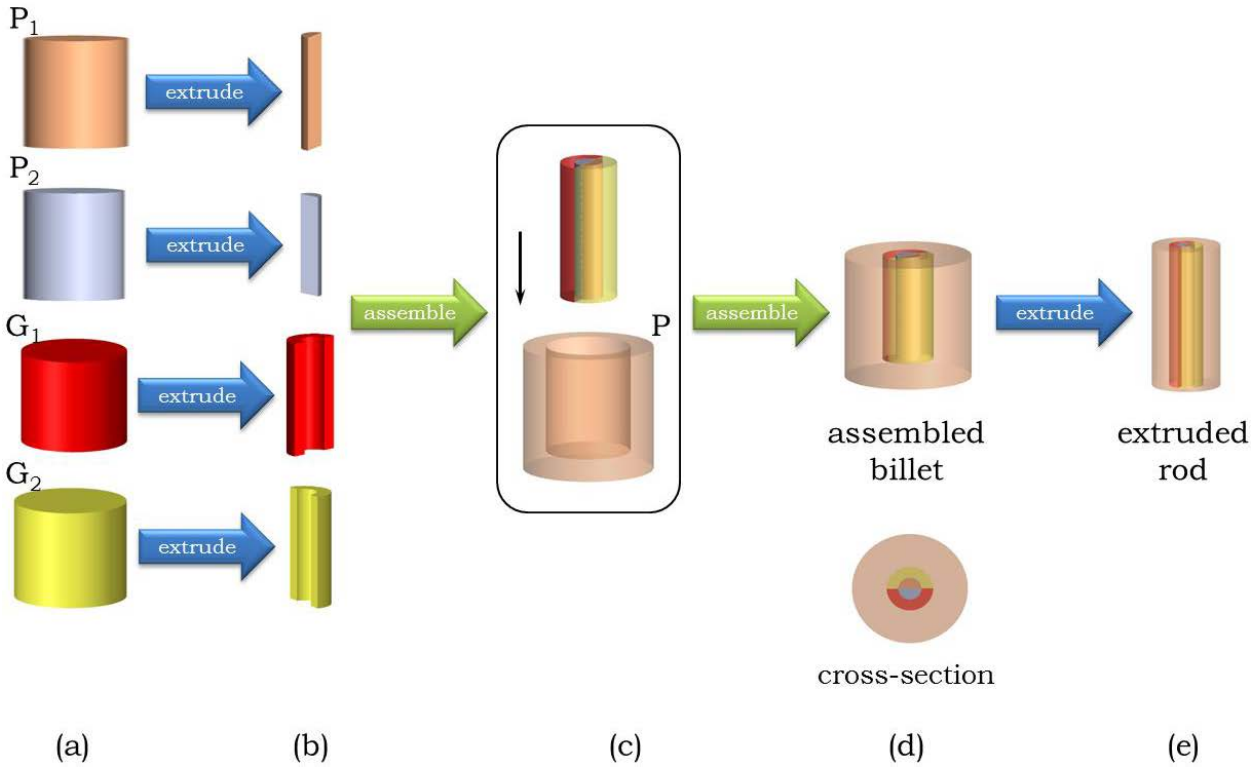

Figure S7 | Preparation of a preform for the double-Janus fiber. (a) Rods of polymers (P_1 and P_2) and glasses (G_1 and G_2) are prepared. (b) The polymer rods are extruded into half cylinders while the glass rods are extruded into half cylindrical tubes. (c) The two polymer half cylinders are assembled into a Janus cylindrical rod, which – in turn – is inserted into the Janus tube formed of the two glass segments. The resulting double-Janus rod is then inserted into a stepped-hole polymer-rod, to form the billet assembly in (d). (e) The billet in (d) is extruded into a cylindrical cane. See text for details.

S2.6 Preform for multi-core particles

A 10-mm-diameter and 100-mm-long G_2 rod was thermally drawn into a 1.5-mm-diameter fiber. A 100-mm-long section of the fiber was inserted into a PES polymer tube (Fig. S8a), and the assembly is thermally consolidated at 250 °C under 10^{-6} Torr vacuum for 30 min (Fig. S8b). The consolidated rod is cut into four 25-mm-long sections whose sides were polished into the shape shown in Fig. 8c. The four sections are stacked together resulting in ~ 3.5-mm core-to-core distance in an assembly with ~ 12-mm outer diameter (Fig. S8d). This assembly is inserted into a G_1 glass tube produced by extrusion (inner diameter = 12 mm, outer diameter = 20 mm, length = 25 mm) and then a PES polymer rod produced by thin-film rolling with a stepped hole (inner diameter = 20 mm, outer diameter = 46 mm, length = 35 mm, hole depth = 25 mm) to form an extrusion billet (Fig. S8e,f). After extrusion, a well-consolidated 10-mm-diameter cane with 4 glass cores embedded in a polymer with one glass cladding and the polymer outer jacket is obtained. A section of the extruded cane is used to prepare a preform drawn into a fiber for particle breakup.

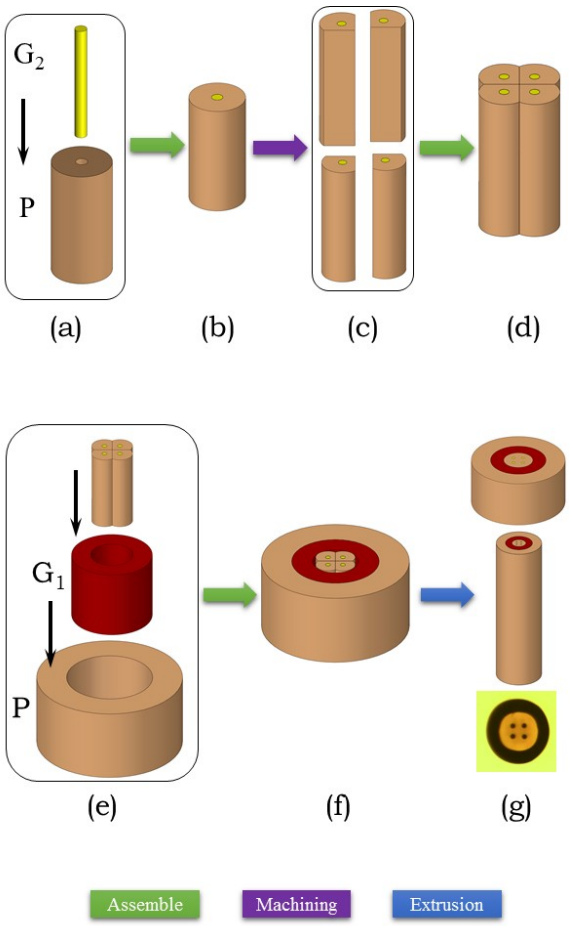

Figure S8 | Preparation of a preform for the 4-core fiber. (a) A G_2 glass rod is thermally drawn into a fibers that is inserted into a polymer tube and (b) consolidated under vacuum. (c)-(d) The consolidated rod is cut into four sections, the sections are side-polished and then stacked. (e)-(f) The stacked assembly is inserted into a G_1 tube and a polymer rod with a stepped hole to form an extrusion billet. (g) After extrusion, a well-consolidated rod with 4 embedded cores is obtained.

S3. Capturing the in-fiber particle formation via the PRI

An optical microscope equipped with a camera (Fig. S9) was used to capture the dynamics of the PRI-breakup in the fibers, as shown in Supplementary Video1 and Video2. The sample is sandwiched between two microscope slides to reduce undesired sample motion while capturing the video. To illuminate the sample, we place an alumina plate under the sample, which scatters onto the sample white light focused from the side via a lens of focal length 50 mm. A 10× microscope objective images light scattered off the sample to the camera (Fig. S10). The sample is heated to 320 °C inside a 2-cm-long heating element mounted on the tip of a soldering iron. Axial modulation along the initially intact cylindrical cores starts after a few minutes, followed by the rapid breakup of the cores located inside the heating zone into spherical particles (which occurs in ~ 30 s); see Fig. S11.

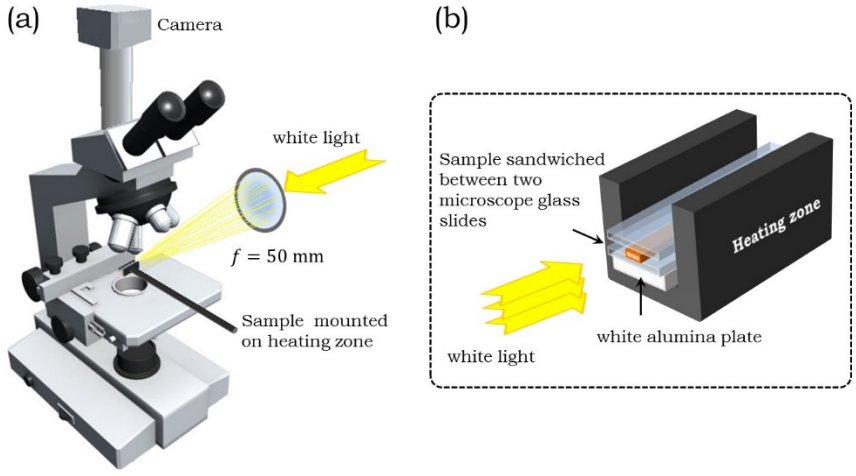

Figure S9 | Configuration for imaging the particle breakup in real-time. (a) Schematic of the optical microscope configuration used to capture the particle breakup videos (Supplementary Video1 and Video2). (b) Detailed view of the sample holder.

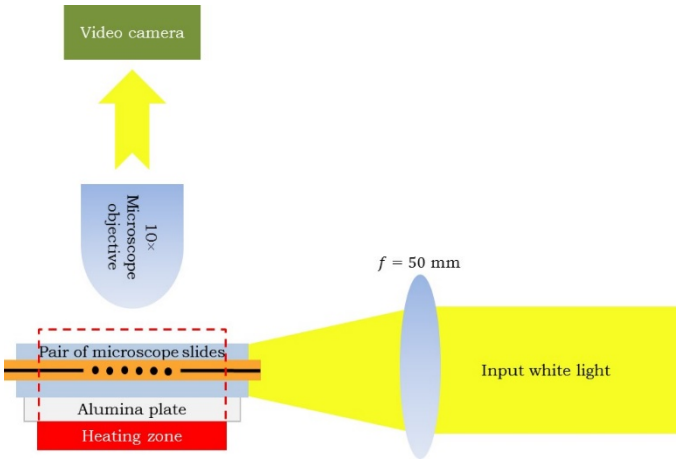

Figure S10 | Side view schematic of the configuration for imaging the particle breakup.

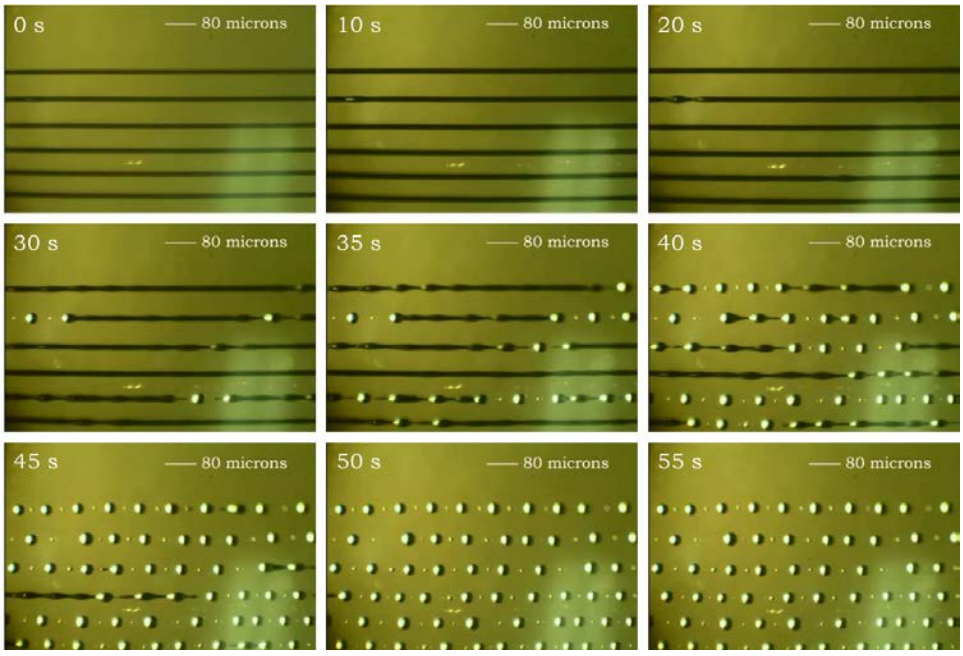

Figure S11 | Breakup dynamics of a multi-core fiber. The panels correspond to successive snapshots from a video (Supplementary Video1; time is indicated in the top-left corner) that capture the breakup dynamics of multiple G_1 glass cores embedded in a PES polymer flat fiber.

S4. Dependence of the breakup dynamics on the core-shell diameter

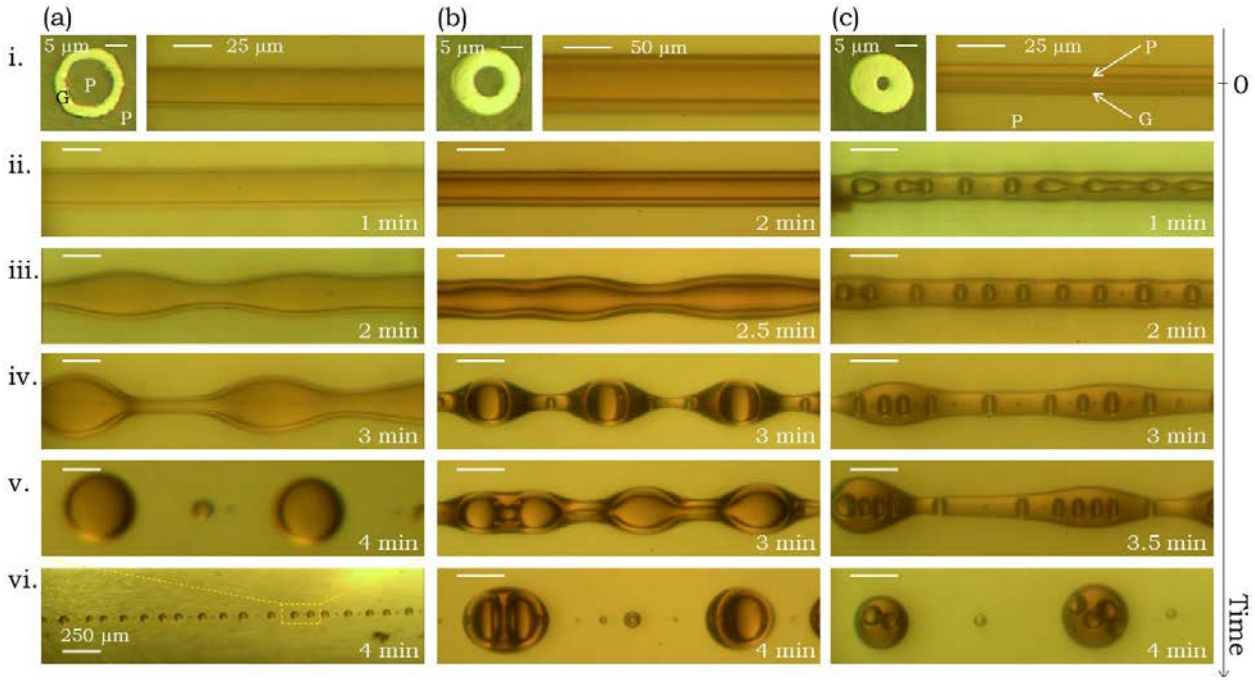

Figure S12 | Dependence of the PRI breakup dynamics of a core-shell fiber on the core-to-shell diameter ratio. (a) Optical reflection micrograph of the fiber cross-section and optical transmission micrograph of the initial fiber side-view (i). The core-to-shell diameter ratio is $\frac{d_{\text{core}}}{d_{\text{shell}}} = 0.7$. Successive rows show optical transmission micrographs of the fiber side-view over time while heating (duration indicated in the bottom-right corner of each panel) to capture the main stages of the PRI-driven breakup dynamics that transforms the cylindrical core into a necklace of spherical particles. (b) Same as (a) for $\frac{d_{\text{core}}}{d_{\text{shell}}} = 0.5$. (c) Same as (a) for $\frac{d_{\text{core}}}{d_{\text{shell}}} = 0.2$.

In Fig. 2 of the main text, we described the breakup of a core-shell spherical particle (polymer core, glass shell) starting from a fiber containing an intact cylindrical core consisting of concentric layers. To obtain the target core-shell structure, fluid dynamics imposes constrains on the allowable ratio of the initial core-to-shell diameters. It is well-established from the classic Tomotika model that the breakup period of a viscous thread embedded in a viscous matrix is proportional to the diameter of the thread [S12]. The breakup period is related to the instability wavelength having the highest growth rate (shortest growth time). If the core diameter is much smaller than that of the shell, then the resulting breakup period of the core may – in turn – be

significantly smaller than that of the shell. Consequently, instead of the desired core-shell structure, multiple smaller core particles are obtained inside a single shell.

These constraints are discussed theoretically in Ref. [S13] and numerically in Ref. [S14]. Here, we present an experimental confirmation of these predictions in Fig. S12. We produce fibers that share the same core structure and are constructed out of the same materials, except that the ratio of the core-to-shell diameters $\frac{d_{\text{core}}}{d_{\text{shell}}}$ are different. We present in Fig. S12 three examples:

1. $\frac{d_{\text{core}}}{d_{\text{shell}}} = 0.7$: Because the core and shell have similar diameters, the target core-shell structure is obtained. The sinusoidal modulations resulting from the PRI along the interfaces occur simultaneously upon heating. Consequently, even the smaller satellite particles that form between the mother particles have a core-shell structure.
2. $\frac{d_{\text{core}}}{d_{\text{shell}}} = 0.5$: Here we start to observe deviations from the target structure. The sinusoidal modulation along the interfaces upon heating are independent to some degree. Consequently, we obtain a subset of particles in which the core-shell structure does not develop. Instead, we sometimes obtain two core particles within the shell. The majority of satellite particles have the core-shell structure.
3. $\frac{d_{\text{core}}}{d_{\text{shell}}} = 0.2$: Here the growth of the sinusoidal instability along the interfaces upon heating are independent. Indeed, the core breaks up into spherical particles before the shell breaks up altogether. As a result, the shells after formation contain several core particles. Furthermore, the satellite particles are formed of the shell material (G_1) only.

Obviously, to reliably produce the desired core-shell structure, one must use $\frac{d_{\text{core}}}{d_{\text{shell}}} > 0.5$. These results are consistent with the numerical simulations shown in Fig. 3E of Ref. [S14], where a crossover between the stable (core-shell) and unstable (multiple cores in a shell) regimes for these classes of materials occurs around the ratio $\frac{d_{\text{core}}}{d_{\text{shell}}} \sim 0.4$.

S5. Experimental details

S5.1 Scattering-strength measurements

The particles are fabricated via the in-fiber PRI as described in the main text and are held in the polymer cladding matrix. The fibers are initially tapered to reach the target diameter. Sections of the fibers are used to extract the particles by first dissolving the polymer cladding using a solvent (Dimethylacetamide, DMAC) at room temperature followed by centrifugation. The particles are then deposited on a cover slip that is placed on the prism.

The intensity distributions were measured across a 10×10 μm^2 plane situated at a height ≈ 2 μm above the particle. For this purpose we used a Nanonics MultiView 4000 tuning-fork near-field scanning optical microscope (NSOM) working in standard collection mode. In tapping mode, we determined the plane of the particle, then retracted the tuning fork 2 □m above tha
experiment, the test particles were placed on the surface of a prism of refractive index $n = 1.5$ and illuminated in total internal reflection by 532-nm-wavelength continuous wave laser beam (100 mW power) slightly focused via a 4× microscope objective, Fig. 3*B*. Scattered light is collected using a Cr-Au coated tapered silica fiber probe (Nanonics) with 50-nm-diameter aperture connected to a photon multiplying tube (PMT; Hamamatsu, H7421). The same neutral density filter was used with all the samples to avoid saturation of the PMT and guarantee that the measurements of the scattered profiles are all on the same intensity scale.

S5.2 Theory for modeling evanescent excitation

To calculate scattering from a spherical particle excited with an evanescent wave, we implemented a complex angle procedure. In this technique, by rotating both the direction and the distribution of the incident electric $\vec{E}(\vec{r}) = \hat{R}_y(-\gamma)\vec{E}\,[\hat{R}_y(\gamma)\vec{r}]$ and magnetic $\vec{H}(\vec{r}) = \hat{R}_y(-\gamma)\vec{H}\,[\hat{R}_y(\gamma)\vec{r}]$) fields by the complex angle γ, a z-propagating plane wave can be transformed into an evanescent field. This transformation was applied to the solution of conventional Mie theory to obtain the evanescent wave scattering from a spherical particle. In the conventional Mie theory, γ defines the orientation of the incident plane wave which is a real quantity; in contrast, γ is a complex angle in the method we employed. In our simulations we adapted a standard Mie scattering code written in MATLAB and included the aforementioned transformation in which the complex angle γ was

obtained as the refraction angle of a plane wave incident on the hypothetical interface between the high-index and low-index media.

S5.3 Polarization measurements

After initiating the PRI and producing the particles, we retain the particles in the fiber and do not dissolve the cladding. As such, the particles all have the same orientation with respect to the fiber axis. The sample is first illuminated with white light to identify and align the particle (Fig. 6*E*,*F*), and then with a green linearly polarized laser (532-nm wavelength) focused at approximately mid-plane of the particle to determine the strength of the polarization-dependent scattering (the horizontal bright lines through the particles in Fig. 6*G*,*H*). Both images are recorded using an Eclipse Ti – Nikon microscope (cooled to -55 °C). With the white light turned off, we imaged the scattered green light across a single particle (Fig. 6*H*) and evaluate the integrated scattered intensity as a function of incident polarization, which is rotated via a half-wave plate (HWP).

References

[S1] Tao, G., Stolyarov, A. M. & Abouraddy, A. F. Multimaterial fibers. *I. J. Appl. Glass Science* **3**, 349–368 (2012).

[S2] Kaufman, J. J., Tao, G., Shabahang, S., Deng, D. S., Fink, Y. & Abouraddy, A. F. Thermal drawing of high-density macroscopic arrays of well-ordered sub-5-nm-diameter nanowires. *Nano Lett.* **11**, 4768–4773 (2011).

[S3] Tao, G., Guo, H., Feng, L., Lu, M., Wei, W. & Peng, B. Formation and properties of a novel heavy-metal chalcogenide glass doped with a high dysprosium concentration. *J. Am. Ceram. Soc*. **92**, 2226–2229 (2009).

[S4] Kaufman, J. J., Tao, G., Shabahang, S., Deng, D. S., Liang, X., Johnson, S. G., Fink, Y. & Abouraddy, A. F. Structured spheres generated by an in-fibre fluid instability. *Nature* **487**, 463–467 (2012).

[S5] Tao, G., Shabahang, S., Banaei, E.-H., Kaufman, J. J. & Abouraddy, A. F. Multimaterial preform coextrusion for robust chalcogenide optical fibers and tapers. *Opt. Lett.* **37**, 2751–2753 (2012).

[S6] Tao, G., Shabahang, S., Ren, H., Yang, Z., Wang, X. & Abouraddy, A. F. Multimaterial rod-in-tube coextrusion for robust mid-infrared chalcogenide fibers. *Proc. SPIE* **8982**, 898223 (2014).

[S7] Tao, G. & Abouraddy, A. F. Multimaterial fibers: a new concept in infrared fiber optics. *Proc. SPIE* **9098**, 90980V (2014).

[S8] Abouraddy, A. F., Bayindir, M., Benoit, G., Hart, S. D., Kuriki, K., Orf, N., Shapira, O., Sorin, F., Temelkuran, B. & Fink, Y. Towards multimaterial multifunctional fibres that see, hear, sense and communicate. *Nat. Mater.* **6**, 336–347 (2007).

[S9] Tao, G., Ebendorff-Heidepriem, H., Stolyarov, A. M., Danto, S., Badding, J. V., Fink, Y., and Ballato, J. & Abouraddy, A. F. Infrared fibers. *Adv. Opt. Photon.* **7**, 379–458 (2015).

[S10] Tao, G., Shabahang, S., Dai, S. & Abouraddy, A. F. Multimaterial disc-to-fiber approach to efficiently produce robust infrared fibers. *Opt. Mat. Express* **4**, 2143–2149 (2014).

[S11] Tao, G., Shabahang, S., Ren, H., Khalizadeh-Rezaie, F., Peale, R. E., Yang, Z., Wang, X. & Abouraddy, A. F. Robust multimaterial tellurium-based chalcogenide glass fibers for mid-wave and long-wave infrared transmission. *Opt. Lett.* **39**, 4009–4012 (2014).

[S12] Tomotika, S. On the instability of a cylindrical thread of a viscous liquid surrounded by another viscous fluid. *Proc. R. Soc. Lond. A* **150**, 322–337 (1935).

[S13] Liang, X., Deng, D. S., Nave, J.-C. & Johnson, S. G. Linear stability analysis of capillary instabilities for concentric cylindrical shells. *J. Fluid Mech.* **683**, 235–262 (2011).

[S14] Kaufman, J. J., Ottman, R., Tao, G., Shabahang, S., Banaei, E.-H., Liang, X., Johnson, S. G., Fink, Y., Chakrabarti, R. & Abouraddy, A. F. In-fiber production of polymeric particles for biosensing and encapsulation. *Proc. Natl. Acad. Science (USA)* **110**, 15549–15554 (2013).